

000 001 002 003 004 005 006 007 008 009 010 011 012 013 014 015 016 017 018 019 020 021 022 023 024 025 026 027 028 029 030 031 032 033 034 035 036 037 038 039 040 041 042 043 044 045 046 047 048 049 050 051 052 053 LOOKUP MULTIVARIATE KOLMOGOROV-ARNOLD NETWORKS

Anonymous authors

Paper under double-blind review

ABSTRACT

High-dimensional linear mappings, or linear layers, dominate both the parameter count and the computational cost of most modern deep-learning models. We introduce lookup multivariate Kolmogorov-Arnold Networks (lmKANs), which deliver a substantially better trade-off between capacity and inference cost. Our construction expresses a general high-dimensional mapping through trainable low-dimensional multivariate functions. These functions can carry dozens or hundreds of trainable parameters each, and yet it takes only a few multiplications to compute them because they are implemented as spline lookup tables. Empirically, lmKANs reduce inference FLOPs by up to $6.0\times$ while matching the flexibility of MLPs in general high-dimensional function approximation. In another feedforward fully connected benchmark, on the tabular-like dataset of randomly displaced methane configurations, lmKANs enable more than $10\times$ higher H100 throughput at equal accuracy. Within the framework of Convolutional Neural Networks, lmKAN-based CNNs cut inference FLOPs at matched accuracy by $1.6\text{--}2.1\times$ and by $1.7\times$ on the CIFAR-10 and ImageNet-1k datasets, respectively.

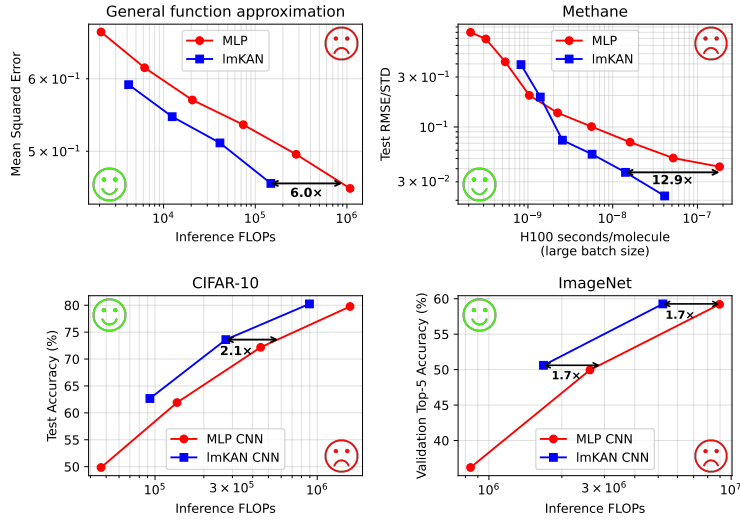


Figure 1: Performance summary. See Sec. 4 for details.

1 INTRODUCTION

With a sufficient amount of training data, the capabilities of deep-learning models systematically improve with the number of trainable parameters (Zhai et al., 2022; Kaplan et al., 2020). However, deploying very large models is challenging because of the associated inference cost.

In most models, high-dimensional linear mappings dominate both the parameter count and the computational cost. Standard multilayer perceptrons (MLPs) alternate linear layers

054 with activations, and sometimes with a few other layers (Ioffe & Szegedy, 2015; Hinton
 055 et al., 2012). If N is the width of a layer, the parameter count and inference cost of these
 056 linear mappings scale as $\mathcal{O}(N^2)$, whereas most other layers scale only as $\mathcal{O}(N)$. The same
 057 observation holds for many other architectures. Transformers (Vaswani et al., 2017), when
 058 applied to very long sequences, are one of the few notable exceptions because the cost of
 059 attention grows quadratically with the number of tokens. Even in that case, however, the
 060 cost of the linear mappings remains substantial, not to mention the potential use of fast
 061 approximations of attention (Choromanski et al., 2020).

062 The computational cost of a linear layer is proportional to the number of its parameters: at
 063 inference, each parameter induces one multiplication per input, where the input is a whole
 064 input object in the case of MLPs, a token in the case of Recurrent Neural Networks (Elman,
 065 1990) and Transformers (Vaswani et al., 2017), a node or an edge in the case of Graph
 066 Neural Networks (Zhou et al., 2020), a patch of an image in the case of Convolutional Neural
 067 Networks (LeCun et al., 2002; Krizhevsky et al., 2012), and similarly for other architectures.

068 Spline lookup tables make it possible to do better than that. Consider, for example, a
 069 one-dimensional piecewise-linear function $f(x)$ on the interval from 0 to 1 with a uniform
 070 grid. On each interval, it is given as $f(x) = a[i] * x + b[i]$, where i is the interval index.
 071 With G intervals, the function has $2G$ parameters, out of which $G + 1$ are independent once
 072 continuity at the internal grid points is enforced. Yet the computational cost of evaluating
 073 such a function at any given point is $\mathcal{O}(1)$, not depending on G . The computational pipeline
 074 involves first determining the current grid interval as $i = \lfloor x * G \rfloor$, and then evaluating only
 075 one linear function as $f(x) = a[i] * x + b[i]$.

076 Kolmogorov-Arnold Networks (KANs) (Liu et al., 2024), designed as a general alternative to
 077 MLPs, are natural hosts for spline lookup tables as they construct a general high-dimensional
 078 mapping through a collection of trainable univariate functions.

079 The main contributions of this work are the following:
 080

- 081 • We propose lookup multivariate Kolmogorov-Arnold Networks (lmKANs) that are
 082 built upon multivariate low-dimensional functions instead of the univariate ones
 083 that standard KANs employ. We empirically compare the 2D version of lmKANs
 084 against 1) 1D FastKAN (Li, 2024b) and 2) 1D version of lmKANs and find that 2D
 085 lmKANs are more accurate and are easier to train in both of the cases.
- 086 • We implement the inner functions as spline lookup tables. Ignoring a non-asymptotic
 087 $\mathcal{O}(N)$ term, the required inference FLOPs are only $2 \times$ those of a linear layer of the
 088 same shape, while the number of trainable parameters can be dozens or hundreds of
 089 times higher.
- 090 • We provide custom CUDA kernels that enable efficient inference of lmKANs on
 091 modern GPUs. When using the 8×8 tile size, on the H100 GPU, our implementation
 092 enables up to $\sim 88 \times$ faster inference compared to a linear layer with the same number
 093 of trainable parameters.
- 094 • We empirically compare lmKANs and MLPs across diverse datasets, scales, and
 095 backbones, using varied experimental setups to obtain a comprehensive view of
 096 performance. Across these conditions, lmKANs are consistently Pareto-optimal with
 097 respect to inference FLOPs. The performance of lmKANs is summarized in Fig. 1.

098 2 RELATED WORK

100 Kolmogorov-Arnold Representation Theorem (KART) (Kolmogorov; Arnold, 2009) states
 101 that a continuous function $f : [0, 1]^n \rightarrow \mathbb{R}$ can be represented as:

$$104 \quad f(x_1, \dots, x_n) = \sum_{q=1}^{2n+1} \Phi_q \left(\sum_{p=1}^n \phi_{q,p}(x_p) \right), \quad (1)$$

105 where $\phi_{q,p} : [0, 1] \rightarrow \mathbb{R}$, and $\Phi_q : \mathbb{R} \rightarrow \mathbb{R}$ are continuous univariate functions. There has been
 106 a long debate (Girosi & Poggio, 1989; Schmidt-Hieber, 2021) on the usefulness of this theorem

108 for machine learning because of the general non-smoothness and wild behavior of the inner
 109 functions. Nevertheless, it inspired the construction of Kolmogorov-Arnold Networks (Hecht-
 110 Nielsen, 1987; Igelnik & Parikh, 2003), whose layers are defined as $y_q = \sum_p f_{qp}(x_p)$, where
 111 f_{qp} are trainable functions. Liu et al. (2024) introduced the modern version, which suggests
 112 stacking an arbitrarily large number of KAN layers and using an arbitrarily large number of
 113 neurons, similarly to MLPs. While Liu et al. (2024) illustrated strong performance of KANs,
 114 many test cases involve ground-truth functions with known, reasonably smooth KART or
 115 KART-like(matching KANs with more than one hidden layer and a larger number of neurons)
 116 closed-form representations. Subsequent works such as Yang & Wang (2024), Kundu et al.
 117 (2024), and Kashefi (2025) further reinforced the efficiency of KANs. On the contrary, Yu
 118 et al. (2024) found that KANs can fall short compared to MLPs for some tasks.
 119

120 The idea of lookup-based $\mathcal{O}(1)$ computations of KAN univariate functions is sometimes
 121 briefly mentioned but rarely implemented in practice (Somvanshi et al., 2024; Ji et al., 2024),
 122 likely because of challenges associated with an efficient GPU implementation. Surprisingly,
 123 most of the research goes in the somewhat opposite direction. B-splines, piecewise polynomial
 124 basis functions used in the original KAN paper, have compact support and thus are well
 125 suited for $\mathcal{O}(1)$ inference. Subsequent works often replace them with dense basis functions,
 126 such as Chebyshev polynomials (SS et al., 2024) or Fourier harmonics (Xu et al., 2024). The
 127 case of FastKAN (Li, 2024b), which replaces sparse B-splines with similar-looking dense
 128 Gaussian radial basis functions exclusively for the sake of optimization, is especially notable.
 129

130 A few works, such as Moradzadeh et al. (2024) and Huang et al. (2025), implement the
 131 lookup idea. Moradzadeh et al. (2024), however, predict B-spline coefficients using an MLP
 132 for the given grid points, which, thus, are not fully independent of each other. Additionally,
 133 it benchmarks **inference cost** against a naive implementation of KANs and not against MLPs,
 134 **thus not claiming that their construction is Pareto optimal compared to MLPs**, which are
 135 still state-of-the-art for general tasks. Huang et al. (2025) achieves remarkable efficiency on
 136 a small-scale problem from the original KAN paper by algorithm-hardware co-design using
 137 the TSMC 22 nm RRAM-ACIM chip. Poluektov & Polar (2025) and Polar & Poluektov
 138 (2021) employ piecewise linear parametrization suitable for $\mathcal{O}(1)$ inference but do not focus
 139 on inference efficiency. While Shtoff (2025) provides a pure PyTorch implementation of
 140 splined parametric curves and, in particular, the KAN architectures derived from them, it
 141 doesn't benefit from the low-level CUDA optimizations as the present work.
 142

143 In this work, we provide CUDA kernels for efficient inference and benchmark the introduced
 144 models against MLPs on general tasks where KART representations are not known in closed
 145 form and where there is no reason to believe that they are smoother than in other cases.
 146

3 LOOKUP MULTIVARIATE KOLMOGOROV-ARNOLD NETWORKS

147 At first glance, given that the inference cost of spline lookup tables does not depend on
 148 the number of parameters, very expressive univariate functions with tens of thousands of
 149 trainable parameters each are an ideal match for the Kolmogorov-Arnold Representation
 150 Theorem. However, KANs rarely use more than a few dozen parameters per function in
 151 practice. The difference between a univariate function parametrized by tens of thousands of
 152 parameters and just a few dozen is the capability of the former to parametrize a very high
 153 frequency band. On the one hand, this expressivity is necessary for closely approximating the
 154 'wild behavior' of KART inner functions, but on the other, it raises concerns about training
 155 stability and generalization. On the contrary, multivariate functions can "accommodate" a
 156 significantly larger number of parameters without spilling expressive power to exceedingly
 157 high frequency bands. For instance, a four-dimensional function with just 10 grid points
 158 along each dimension has roughly the same number of trainable parameters as a univariate
 159 one with $\sim 10^4$ grid intervals.

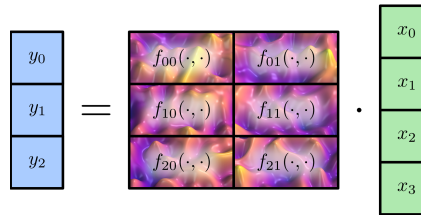
160 A layer of a multivariate version of Kolmogorov-Arnold Networks with dimension d defines
 161 the output as:

$$y_q = \sum_{p=0}^{N_{\text{in}}/d-1} f_{qp}(x_{dp}, x_{dp+1}, \dots, x_{dp+d-1}), \quad (2)$$

162 where f_{qp} are trainable d -dimensional functions and N_{in} is the input dimensionality (assumed
 163 to be divisible by d). We implement CUDA kernels for the [one- and two-dimensional cases](#).
 164 The motivation behind this choice is detailed in Section 3.2. An example of such a layer
 165 in the 2D case is depicted in Fig. 2. Similar to KANs, these layers do not need additional
 166 activations in between and can be stacked arbitrarily, substituting linear mapping-activation
 167 pairs in MLP-based backbones.

168 In Sec. 4.4, we empirically compare the two-dimensional version of lmKANs with [both](#)
 169 [one-dimensional lmKAN](#) and [one-dimensional FastKAN](#). The outcomes of these numerical
 170 experiments reinforce the intuitive considerations given here and suggest that multidimen-
 171 sional building blocks can indeed be more effective hosts for a large number of parameters in
 172 a practical setup.

173 Additionally, it is worth noting that, if necessary, multivariate functions f_{qp} can always
 174 fall back to sums of univariate ones, which would make the whole lmKAN fall back to
 175 standard KAN. Thus, the Kolmogorov-Arnold Representation Theorem is applicable also to
 176 our construction.



186 Figure 2: Schematic representation of a 2D lmKAN layer with 4 inputs and 3 outputs. This
 187 layer defines outputs as: $y_0 = f_{00}(x_0, x_1) + f_{01}(x_2, x_3)$, $y_1 = f_{10}(x_0, x_1) + f_{11}(x_2, x_3)$, and
 188 $y_2 = f_{20}(x_0, x_1) + f_{21}(x_2, x_3)$. The functions $f_{**}(\cdot, \cdot)$ are to be trained during fitting.

190 3.1 FUNCTION PARAMETRIZATION

192 During training, activations of neurons can evolve arbitrarily, making the use of grids defined
 193 on bounded regions challenging. Therefore, we designed an unbounded grid which is still
 194 regular enough to allow $\mathcal{O}(1)$ computations.

196 **Sigma grid** The one-dimensional sigma grid, which is illustrated in the left panel of Fig. 3,
 197 is generated by any sigmoid-like function $\sigma(x)$. If the desired number of grid intervals is
 198 G , then the grid points are given as the intersection of $G - 1$ equispaced percentile levels
 199 with $\sigma(x)$. Such a construction spans the entire real axis. The grid has the finest resolution
 200 near the origin, and becomes progressively coarser as $|x|$ increases. For a given x , the
 201 index of the corresponding grid interval can be computed as $i = \lfloor \sigma(x)G \rfloor$, which makes
 202 such a grid suitable for $\mathcal{O}(1)$ computations. For multivariate functions, we apply the same
 203 one-dimensional grid independently to each coordinate.

204 To balance occupancy across intervals, we precede each lmKAN layer with batch normalization
 205 without affine parameters to keep the activations in the controlled range. The choice of the
 206 $\sigma(x)$ function was primarily motivated by computational efficiency. The exact definition and
 207 other details are available in Appendix B.

209 **Compact basis functions** We use B-splines of second order built on top of the described
 210 grid as basis functions to parametrize the lmKAN inner functions. A one-dimensional
 211 second-order B-spline centered around grid point i is given in the right panel of Fig. 3.
 212 It takes non-zero values on only two adjacent grid intervals around the center grid point.
 213 If there are G intervals, then we use $G + 1$ basis functions: $G - 1$ such B-splines cen-
 214 tered around each inner grid point, and two linear functions on the leftmost and right-
 215 most infinite intervals. Appendix B provides the definition of B-splines on edge intervals
 we use in this work, along with other details. A two-dimensional B-spline is defined

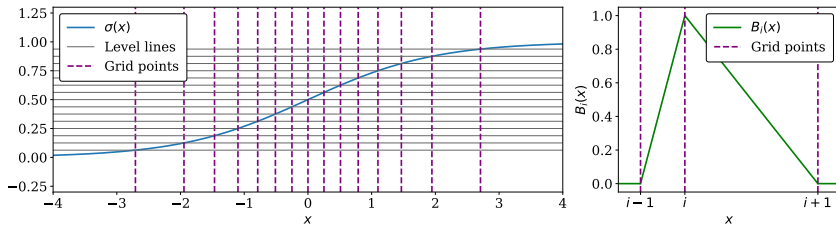
216
217
218
219
220
221
222
223

Figure 3: (Left) Construction of the sigma grid; (Right) Second-order B-spline.

224
225
226

227 as $B_{i_1 i_2}(x_1, x_2) = B_{i_1}(x_1) B_{i_2}(x_2)$. All the functions defining a 2D lmKAN layer are
228 parametrized as $f(x_1, x_2) = \sum_{i_1, i_2} p_{i_1 i_2} B_{i_1 i_2}(x_1, x_2)$, where $p_{i_1 i_2}$ are trainable coefficients.
229

230 With such a construction, there are $(G + 1)^2$ independent parameters for each 2D function,
231 parametrized functions are bilinear on each 2D grid interval, all the functions are continuous
232 for arbitrary $p_{i_1 i_2}$, and all but the edge coefficients $p_{i_1 i_2}$ have a simple interpretation of the
233 value of the function on the corresponding grid point.

234 For any given point (x_1, x_2) , there are only four non-zero B-splines; thus, one needs to evaluate
235 only four terms to compute $f(x_1, x_2)$, which forms the basis of $\mathcal{O}(1)$ computations. The full
236 algorithm to compute a standalone two-dimensional function is given in Appendix B.1.

237

238

3.2 COMPUTATIONAL COST

239

240 Overall, the functional form of lmKANs involves computations of many low-dimensional
241 functions with exactly the same arguments (those in the same column, see Fig. 2). When
242 doing so, it is possible to reuse many of the intermediate values, such as indices of the
243 grid intervals and B-splines. These intermediate values can be computed once for each
244 pair of inputs, and then utilized to compute the value of a given function with just four
245 multiply-add operations for the 2D case. Given that the total number of 2D functions in
246 an lmKAN layer is $[N_{\text{in}}/2]N_{\text{out}}$, the total number of required multiply-add operations for
247 the dominant, $\mathcal{O}(N^2)$, part is $4[N_{\text{in}}/2]N_{\text{out}} = 2N_{\text{in}}N_{\text{out}}$, just $2\times$ that of a linear layer of the
248 same shape. Algorithm 3, given in Appendix C, pinpoints this estimation. Following the
249 common practice (He et al., 2016), we estimate FLOPs as the number of fused multiply-adds
of the main asymptotic term for both MLPs and lmKANs.

250

251 It is worth noting that the non-asymptotical $\mathcal{O}(N)$ term is not an additional cost relative to
252 MLPs; it replaces the per-unit bias additions and activation evaluations that lmKANs do not
253 require — operations that can be quite expensive when the activations are transcendental
functions such as \tanh .

254

255

3.3 PERSPECTIVE ON DIMENSIONS AND SPLINE ORDERS

256

257 All the constructions introduced so far straightforwardly generalize to a higher-dimensional
258 case. Evaluation of a single d -dimensional function parametrized by d -dimensional second-
259 order B-splines would take 2^d multiply-adds, which stem from the summation of B-spline
260 contributions residing on all the corners of the corresponding d -dimensional hypercube.
261 Given that the number of such d -dimensional functions would be d times smaller compared
262 to the number of weights of a linear layer of the same shape, the inference FLOPs of the
263 d -dimensional lmKAN layer would be $2^d/d$ of that of the linear layer with the same shape.

264

265 These slowdown factors are identical, $2\times$, for one- and two-dimensional lmKANs, and start
266 to grow for higher dimensions. Thus, we chose the one- and two-dimensional versions for
267 the implementation of CUDA kernels as the 2D extension of the standard univariate KAN
comes essentially for free.

268

269 If B-splines of order k are employed for parametrization instead of the second-order ones
described so far, the inference cost becomes k^d/d of that of MLP. For more details, see the
B-spline definition at De Boor & De Boor (1978), and how they are used in KANs (Liu et al.,

2024). Increasing the B-spline order brings a few benefits, but they likely do not justify the associated increase in the computational cost.

The classical theorem about B-splines (De Boor, 1968) indicates that while the order of B-splines affects the convergence rate, any spline order is sufficient to approximate any function arbitrarily close by increasing the resolution of the grid¹. Given that the computational cost of spline look-up tables does not depend on the number of grid points, the grid resolution can be arbitrarily increased without any computational overhead at inference.

On top of that, increasing the B-spline order introduces additional smoothness of the model. Functions parametrized by B-splines of order k belong to C^{k-2} , but in general not to C^{k-1} . The smoothness of second-order B-splines employed in this work matches that of ReLU (Glorot et al., 2011), one of the most popular and successful activation functions, which is also continuous, but not continuously differentiable. Thus, it is questionable if the additional smoothness available through higher orders k is necessary and would justify the associated computational overhead.

3.4 CUDA KERNELS

We implement CUDA kernels for efficient inference of 1D and 2D lmKANs on modern GPUs. Our kernels use the classic shared memory tiling used in GEMM (Volkov & Demmel, 2008). In the following, all benchmarks run in full-precision `float32`.

In the 2D case, with a 16×16 tile, our implementation is $\sim 8 \times$ slower than a dense linear layer with the same shape on an H100-SXM, irrespective of the grid resolution. The slowdown exceeds the $\sim 2 \times$ FLOPs-based estimate from Sec. 3.2, primarily because of the less coherent memory-access pattern of algorithm 3. Additionally, dense matrix multiplication has been the cornerstone of many computational pipelines and, thus, has enjoyed decades of thorough optimization.

Finite shared memory capacity limits the number of grid intervals to $G \leq 20$ on H100. At this limit, an lmKAN layer holds $(20 + 1)^2 / 2 \approx 220 \times$ more parameters than the linear baseline with the same shape. It means that an lmKAN layer delivers $[(20 + 1)^2 / 2] / 8 \approx 27.5 \times$ **faster** inference compared to a linear layer with the same number of trainable parameters.

Reducing the tile to 8×8 raises the slowdown to $\sim 9.5 \times$ but lets us increase G to 40, yielding $\approx 88.5 \times$ better per-parameter efficiency.

4 RESULTS

We have demonstrated so far that lmKANs can have significantly better inference cost per trainable parameter compared to linear layers in terms of both FLOPs and wall-clock time on modern GPUs. The question is, however, whether this nominal efficiency translates to real-life performance. Do lmKANs indeed represent a better tradeoff between performance and inference cost?

In this section, we empirically compare the efficiency of lmKANs and MLPs across the following settings: (i) approximating general high-dimensional functions, (ii) on a tabular-like dataset of randomly displaced methane configurations, and (iii) within CNN frameworks evaluated on CIFAR-10 and ImageNet. Across all experiments, we use identical macro-architectural backbones for lmKANs and MLPs. Overall, to obtain a comprehensive picture of the performance, we prioritized the diversity of the setups over a very large scale or the architectural complexity of a particular backbone. We found that lmKANs are consistently inference FLOPs — accuracy Pareto-optimal, with the largest gains on the methane dataset. Finally, we compare lmKANs with FastKANs.

4.1 GENERAL FUNCTION APPROXIMATION

Our first experiment is set to measure crude flexibility of ImKANs in approximating general high-dimensional functions, which we model by large teacher MLPs with fixed random

¹This is applicable, though, to functions on a bounded domain.

weights. We define a ground-truth $\mathbb{R}^{32} \rightarrow \mathbb{R}^1$ function as an MLP with 32 input neurons, 10 hidden layers, each with 1024 neurons, and hyperbolic tangent activations.

We fit both MLP and lmKAN students to approximate this ground-truth function and compare their performance. We use the same fully connected backbone for both types of models with two hidden layers and varying hidden dimensions and grid resolutions G , see more details in Appendix G.2.

In our first experiment, we fixed the hidden dimension at 256 to investigate the performance of 1D and 2D lmKANs as a function of grid resolution G . The results, presented in Fig. 4 (left panel), show that performance does not improve indefinitely with higher resolution; instead, it follows a U-shaped curve. However, there is a notable distinction between the one- and two-dimensional cases: the 2D lmKAN saturates at a much larger number of trainable parameters per function and achieves significantly higher accuracy. Notably, the 2D lmKAN with optimal grid resolution performs comparably to an MLP that is roughly 16 times larger (with a $4 \times$ larger hidden dimension). Furthermore, the second and third panels confirm that inference cost—in terms of both FLOPs and H100 SXM wall-clock time—remains independent of the grid resolution G .

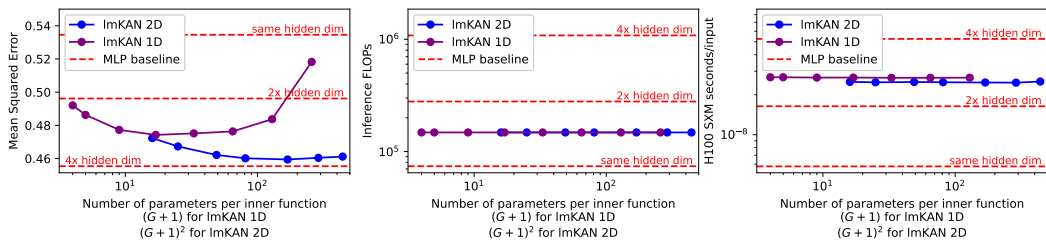


Figure 4: Performance of 1D and 2D lmKANs depending on the grid resolution.

In our second experiment, we fixed the grid resolution at its optimal value and varied the hidden dimensions for both MLPs and 2D lmKANs. As expected, the final Mean Squared Error (MSE) decreases monotonically with the hidden dimension, reflecting the increased flexibility of the models. However, larger hidden dimensions inevitably incur higher inference costs; the key question, therefore, is which architecture offers a better tradeoff between accuracy and efficiency. Our findings are summarized in Fig. 5. The left panel plots the final MSE against the hidden dimension, while the middle and right panels depict the Pareto fronts for MSE versus inference FLOPs and H100 wall-clock time, respectively.

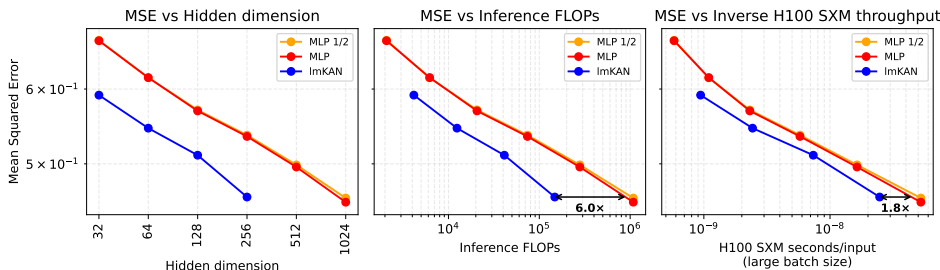


Figure 5: lmKAN vs MLP for general function approximation. The "MLP 1/2" line corresponds to the outcome of the fitting procedure with only half of the training steps compared to the "MLP" one.

In order to justify the claims that lmKANs are indeed more efficient, we converge baseline MLP-based models very tightly here, and in all similar experiments in this manuscript. For the MLP baseline, we have two lines - one with a full training budget and one with only half of it. The close similarity between them demonstrates very tight convergence.

378 Fig. 5 clearly indicates that lmKANs are significantly more FLOPs efficient at the same
 379 accuracy level, up to $6\times$, for the largest dimensions. Furthermore, lmKANs also appeared
 380 to be H100 wall-clock time optimal for all the scales, with the speedup factor of about $1.8\times$
 381 for the largest hidden dimension.

382 Appendix G.2 contains analogous experiment for an $\mathbb{R}^{32} \rightarrow \mathbb{R}^{32}$ function, ablation studies,
 383 and other details.
 384

385 4.2 RANDOMLY DISPLACED METHANE CONFIGURATIONS

387 Having demonstrated that lmKANs are Pareto-optimal when approximating a general function, we proceed to benchmark their
 388 efficiency on real data. We chose the tabular-like dataset of randomly displaced methane configurations for the comparison, as it
 389 is particularly suitable for this purpose (see Appendix G.4). The dataset consists of multiple off-equilibrium methane configurations,
 390 as illustrated in Fig. 6. The target is given by the corresponding quantum-mechanical energy (Turney et al., 2012; Kohn & Sham,
 391 1965). Hydrogen atoms are placed around the carbon atom randomly, varying from instance to instance, which leads to different
 392 target energies.
 393

398 We encode the geometry of each methane molecule by the Cartesian
 399 components of displacement vectors from the carbon atom to all
 400 the hydrogen atoms. Therefore, the input dimension of both the
 401 lmKAN and the MLP networks is 12. Otherwise, we use the same
 402 backbone with two hidden layers as in the previous experiment.

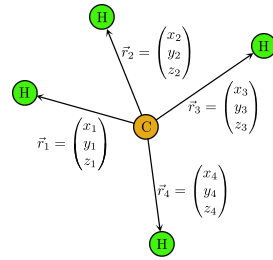
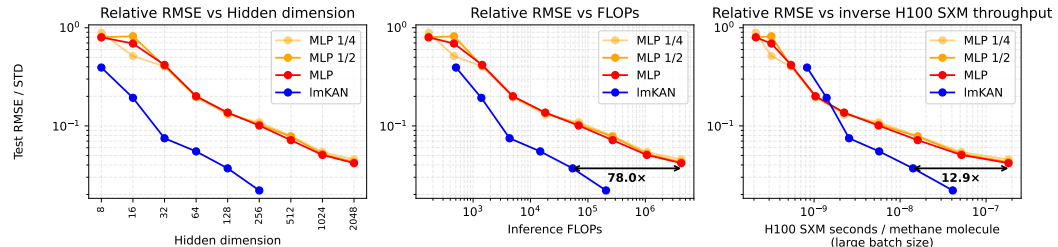


Figure 6: A methane configuration



413 Figure 7: lmKAN vs MLP on the dataset of randomly displaced methane configurations.
 414 On the vertical axis, we plot the relative Root Mean Squared Error, which is given as test
 415 RMSE normalized by the standard deviation of the target in the dataset. The "MLP 1/2"
 416 and "MLP 1/4" curves correspond to outcomes of fitting procedures with half and a quarter
 417 of the training budget, respectively.

418 Our findings are given in Fig. 7. Similar to the previous experiment, lmKANs were found to
 419 be Pareto-optimal in terms of both formal FLOPs and H100 wall-clock time. Moreover, the
 420 relative speedup is higher for this dataset: up to $78.0\times$ reduced FLOPs, and $12.9\times$ faster
 421 H100 inference at matched accuracy.

423 In Appendix G.4 we provide ablation studies, analogous experiments using representations
 424 other than the Cartesian components of the displacement vectors, and further details.

425 4.3 IMKAN-BASED CONVOLUTIONAL NEURAL NETWORKS

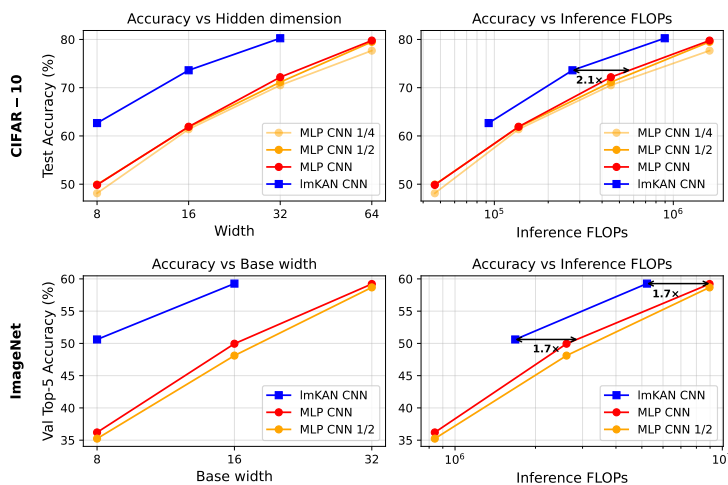
427 In the introduction, we briefly outlined that high-dimensional linear mappings are the
 428 primary building blocks in most architectures, not only in feedforward fully connected neural
 429 networks. Convolutional Neural Networks (CNNs) are no exception.

431 A standard two-dimensional convolution with kernel size $k \times k$ is parametrized by linear
 432 mapping $\mathbb{R}^{k^2 C_{in}} \rightarrow \mathbb{R}^{C_{out}}$, where C_{in} and C_{out} are numbers of input and output channels,

432 respectively. Since Kolmogorov-Arnold layers can be used as a general substitute for high-
 433 dimensional linear mappings, one can construct a KAN-based convolutional neural network
 434 well suited for image processing, as was done, e.g., in Bodner et al. (2024). In this section, we
 435 compare the performance of lmKAN- and MLP-based CNNs on the CIFAR-10 (Krizhevsky
 436 et al., 2009) and ImageNet (Deng et al., 2009) datasets.

437 For CIFAR-10, our backbone architecture consists of five 2×2 convolutions, each with stride
 438 2, and two fully connected layers at the end. We use identical backbones for lmKAN and
 439 MLP CNNs, and exactly the same pool of augmentations, see more details in Appendix G.5.
 440 Similarly to the previous experiments, we vary the width of the neural networks, which is
 441 the number of filters in the case of convolutions, and the hidden dimension in the case of
 442 fully connected layers.

443 For ImageNet, we downsample the images to a resolution of 81×81 pixels. Our backbone
 444 consists of four convolutional layers with the 3×3 kernel size and stride 3 and two fully
 445 connected layers. In contrast to the CIFAR-10 experiment, we progressively increase the
 446 number of filters as the spatial resolution of the image decreases through the neural network.
 447



464 Figure 8: Comparison of the performance of standard MLP-based CNNs and lmKAN-based
 465 CNNs on the CIFAR-10 and ImageNet datasets. The "MLP CNN 1/2" line corresponds to
 466 the outcome of the fitting procedure with only half of the training steps compared to the
 467 "MLP CNN" one.

468 Our findings are illustrated in Fig. 8. Similarly to previous experiments, lmKAN-based
 469 CNNs were found to be more FLOPs efficient at the same accuracy level. The observed
 470 reduction in FLOPs is 1.6-2.1 \times for CIFAR-10, and 1.7 \times for ImageNet. We have not yet
 471 implemented dedicated CUDA kernels for efficient inference of lmKAN-based convolutions.
 472 Any type of convolution can be cast to a fully connected layer by the corresponding memory
 473 manipulations, which we employed during fitting.

475 4.4 COMPARISON WITH FASTKAN

477 In this section, we compare the performance of 2D lmKAN, 1D lmKAN, and FastKAN models.
 478 We use the training script² for the CIFAR-10 dataset available in the FastKAN GitHub
 479 repository (Li, 2024a), as the basis for the comparison. This script fits a fully connected
 480 FastKAN model with one hidden layer. We provide several modifications, particularly
 481 enabling the same augmentation pipeline we used in the previous section (Appendix G.6).

482 We fixed the hidden dimensionality of 256 as in the original script for all the models and vary
 483 grid resolutions and analyze the accuracy depending on the number of trainable parameters
 484 in each inner function. The result is given in Fig. 9.

485 ²https://github.com/ZiyaoLi/fast-kan/blob/master/examples/train_cifar10.py

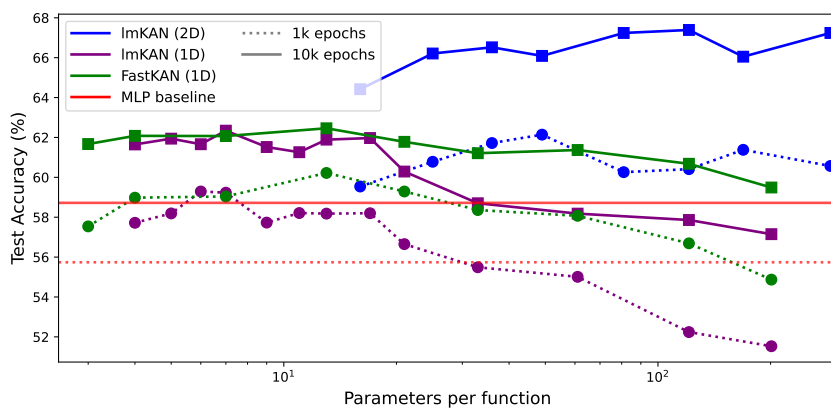


Figure 9: Comparison of the one- and two-dimensional lmKAN and FastKAN models within the fully connected framework on the CIFAR-10 dataset for fitting budgets of one and ten thousand epochs. The number of parameters per inner function is $(G + 1)^2$ for 2D lmKAN, $(G + 1)$ for 1D lmKAN, and $(\text{num_grids} + 1)$ for FastKAN.

The first observation is that the performance of **both FastKAN and 1D lmKAN** models degrades for excessively fine grid resolutions. For the training budget of one thousand epochs, the final models becomes even less accurate than the MLP baseline. For ten thousand epochs, the effect is less pronounced, but it still takes place. This degradation is much less severe, if present at all, for the **2D lmKAN** models - they are easier to fit even for a very rich parametrization of each inner function. Another distinct feature of Fig. 9 is that **2D lmKANs** achieve notably better accuracy compared to both **1D lmKANs and FastKANs**, even when the latter have a very rich parametrization of inner functions.

To sum up, these findings reinforce the intuitive considerations given in Sec. 3 and suggest that building blocks of multivariate trainable functions are indeed more effective.

5 SUMMARY

High-dimensional linear mappings are the cornerstone of modern deep learning, dominating both the parameter count and the computational cost in most models. We introduce lookup multivariate Kolmogorov-Arnold Networks (lmKANs) that offer a substantially better capacity–inference cost ratio. Across all experiments, lmKANs were found to be inference FLOPs Pareto-optimal. The efficiency gains are task-dependent: for general high-dimensional function approximation, modelled as a distillation from a large ground truth teacher MLP with random weights, lmKANs achieved up to $6\times$ fewer FLOPs at matched accuracy. On randomly displaced methane configurations, efficiency improved by up to $78\times$. Within convolutional networks, the gains were smaller but still significant: $1.6\text{--}2.1\times$ on CIFAR-10 and $1.7\times$ on ImageNet.

Our CUDA kernels compete directly with highly optimized dense matrix multiplications—the backbone of many numerical pipelines for decades. Even so, the gains were sufficient to make lmKANs Pareto-optimal in H100 wall-clock time for both the general high-dimensional function approximation and the methane dataset, achieving the speedup of more than an order of magnitude in the latter case.

540 6 REPRODUCIBILITY STATEMENT
541542 The associated supplementary material contains not only the implementation of lmKANs,
543 but also training scripts for the experiments presented in this manuscript, along with the
544 corresponding settings as a collection of YAML files. These assets enable reproducibility of
545 the numerical experiments presented in this paper.546
547 7 ETHICS STATEMENT
548549 This work adheres to the ethical standards expected at ICLR 2026. To the best of our
550 knowledge, the proposed method is not expected to have adverse effects.
551552 REFERENCES
553554 Alice EA Allen, Geneviève Dusson, Christoph Ortner, and Gábor Csányi. Atomic permuta-
555 tionally invariant polynomials for fitting molecular force fields. *Machine Learning: Science
556 and Technology*, 2(2):025017, 2021.557 Vladimir I Arnold. On functions of three variables. *Collected Works: Representations of
558 Functions, Celestial Mechanics and KAM Theory, 1957–1965*, pp. 5–8, 2009.
559560 Albert P Bartók, Mike C Payne, Risi Kondor, and Gábor Csányi. Gaussian approximation
561 potentials: The accuracy of quantum mechanics, without the electrons. *Physical review
562 letters*, 104(13):136403, 2010.563 Jörg Behler and Michele Parrinello. Generalized neural-network representation of high-
564 dimensional potential-energy surfaces. *Physical review letters*, 98(14):146401, 2007.
565566 Alexander Dylan Bodner, Antonio Santiago Tepsich, Jack Natan Spolski, and Santiago
567 Pourteau. Convolutional kolmogorov-arnold networks. *arXiv preprint arXiv:2406.13155*,
568 2024.569 Krzysztof Choromanski, Valerii Likhoshesterov, David Dohan, Xingyou Song, Andreea Gane,
570 Tamas Sarlos, Peter Hawkins, Jared Davis, Afroz Mohiuddin, Lukasz Kaiser, et al. Re-
571 thinking attention with performers. *arXiv preprint arXiv:2009.14794*, 2020.
572573 Ekin D Cubuk, Barret Zoph, Jonathon Shlens, and Quoc V Le. Randaugment: Practical au-
574 tomated data augmentation with a reduced search space. In *Proceedings of the IEEE/CVF
575 conference on computer vision and pattern recognition workshops*, pp. 702–703, 2020.576 George Cybenko. Approximation by superpositions of a sigmoidal function. *Mathematics of
577 control, signals and systems*, 2(4):303–314, 1989.
578579 Carl De Boor. On uniform approximation by splines. *J. Approx. Theory*, 1(1):219–235, 1968.580 Carl De Boor and Carl De Boor. *A practical guide to splines*, volume 27. Springer New York,
581 1978.
582583 Jia Deng, Wei Dong, Richard Socher, Li-Jia Li, Kai Li, and Li Fei-Fei. Imagenet: A large-scale
584 hierarchical image database. In *2009 IEEE conference on computer vision and pattern
585 recognition*, pp. 248–255. Ieee, 2009.586 Harm Derksen and Gregor Kemper. *Computational invariant theory*. Springer, 2015.
587588 Jeffrey L Elman. Finding structure in time. *Cognitive science*, 14(2):179–211, 1990.589 Federico Girosi and Tomaso Poggio. Representation properties of networks: Kolmogorov’s
590 theorem is irrelevant. *Neural Computation*, 1(4):465–469, 1989.
591592 Xavier Glorot, Antoine Bordes, and Yoshua Bengio. Deep sparse rectifier neural networks.
593 In *Proceedings of the fourteenth international conference on artificial intelligence and
statistics*, pp. 315–323. JMLR Workshop and Conference Proceedings, 2011.

594 David Harrison Jr and Daniel L Rubinfeld. Hedonic housing prices and the demand for clean
 595 air. *Journal of environmental economics and management*, 5(1):81–102, 1978.
 596

597 Kaiming He, Xiangyu Zhang, Shaoqing Ren, and Jian Sun. Deep residual learning for
 598 image recognition. In *Proceedings of the IEEE conference on computer vision and pattern
 599 recognition*, pp. 770–778, 2016.

600 Robert Hecht-Nielsen. Kolmogorov’s mapping neural network existence theorem. In *Proceed-
 601 ings of the international conference on Neural Networks*, volume 3, pp. 11–14. IEEE press
 602 New York, NY, USA, 1987.
 603

604 Geoffrey E Hinton, Nitish Srivastava, Alex Krizhevsky, Ilya Sutskever, and Ruslan R
 605 Salakhutdinov. Improving neural networks by preventing co-adaptation of feature detectors.
 606 *arXiv preprint arXiv:1207.0580*, 2012.

607 Wei-Hsing Huang, Jianwei Jia, Yuyao Kong, Faaiq Waqar, Tai-Hao Wen, Meng-Fan Chang,
 608 and Shimeng Yu. Hardware acceleration of kolmogorov-arnold network (kan) for lightweight
 609 edge inference. In *Proceedings of the 30th Asia and South Pacific Design Automation
 610 Conference*, pp. 693–699, 2025.

611 Boris Igelnik and Neel Parikh. Kolmogorov’s spline network. *IEEE transactions on neural
 612 networks*, 14(4):725–733, 2003.
 613

614 Sergey Ioffe and Christian Szegedy. Batch normalization: Accelerating deep network training
 615 by reducing internal covariate shift. In *International conference on machine learning*, pp.
 616 448–456. pmlr, 2015.
 617

618 Tianrui Ji, Yuntian Hou, and Di Zhang. A comprehensive survey on kolmogorov arnold
 619 networks (kan). *arXiv preprint arXiv:2407.11075*, 2024.

620 Kaggle. Titanic — machine learning from disaster. [https://www.kaggle.com/](https://www.kaggle.com/competitions/titanic)
 621 [competitions/titanic](https://www.kaggle.com/competitions/titanic). Accessed 2025-08-19.
 622

623 Jared Kaplan, Sam McCandlish, Tom Henighan, Tom B Brown, Benjamin Chess, Rewon
 624 Child, Scott Gray, Alec Radford, Jeffrey Wu, and Dario Amodei. Scaling laws for neural
 625 language models. *arXiv preprint arXiv:2001.08361*, 2020.

626 Ali Kashefi. Pointnet with kan versus pointnet with mlp for 3d classification and segmentation
 627 of point sets. *Computers & Graphics*, pp. 104319, 2025.
 628

629 Walter Kohn and Lu Jeu Sham. Self-consistent equations including exchange and correlation
 630 effects. *Physical review*, 140(4A):A1133, 1965.

631 Andrei Kolmogorov. *On the representation of continuous functions of several variables by
 632 superpositions of continuous functions of a smaller number of variables*.
 633

634 Alex Krizhevsky, Geoffrey Hinton, et al. Learning multiple layers of features from tiny
 635 images. 2009.

636 Alex Krizhevsky, Ilya Sutskever, and Geoffrey E Hinton. Imagenet classification with deep
 637 convolutional neural networks. *Advances in neural information processing systems*, 25,
 638 2012.

639 Akash Kundu, Aritra Sarkar, and Abhishek Sadhu. Kanqas: Kolmogorov-arnold network for
 640 quantum architecture search. *EPJ Quantum Technology*, 11(1):76, 2024.
 641

642 Yann LeCun, Léon Bottou, Yoshua Bengio, and Patrick Haffner. Gradient-based learning
 643 applied to document recognition. *Proceedings of the IEEE*, 86(11):2278–2324, 2002.
 644

645 Ziyao Li. fast-kan: Fastkan — very fast implementation of kolmogorov-arnold networks
 646 (kan). <https://github.com/ZiyaoLi/fast-kan>, 2024a. GitHub repository.
 647

Ziyao Li. Kolmogorov-arnold networks are radial basis function networks. 2024b.

648 Ziming Liu, Yixuan Wang, Sachin Vaidya, Fabian Ruehle, James Halverson, Marin Soljačić,
 649 Thomas Y Hou, and Max Tegmark. Kan: Kolmogorov-arnold networks. *arXiv preprint*
 650 *arXiv:2404.19756*, 2024.

651 Ilya Loshchilov and Frank Hutter. Sgdr: Stochastic gradient descent with warm restarts.
 652 *arXiv preprint arXiv:1608.03983*, 2016.

654 Alireza Moradzadeh, Lukasz Wawrzyniak, Miles Macklin, and Saeed G Paliwal. Ukan:
 655 Unbound kolmogorov-arnold network accompanied with accelerated library. *arXiv preprint*
 656 *arXiv:2408.11200*, 2024.

657 Andrew Polar and Michael Poluektov. A deep machine learning algorithm for construction of
 658 the kolmogorov-arnold representation. *Engineering Applications of Artificial Intelligence*,
 659 99:104137, 2021.

661 Michael Poluektov and Andrew Polar. Construction of the kolmogorov-arnold networks using
 662 the newton-kaczmarz method. *Machine Learning*, 114(8):185, 2025.

663 Sergey Pozdnyakov and Michele Ceriotti. Smooth, exact rotational symmetrization for
 664 deep learning on point clouds. *Advances in Neural Information Processing Systems*, 36:
 665 79469–79501, 2023.

667 Johannes Schmidt-Hieber. The kolmogorov-arnold representation theorem revisited. *Neural*
 668 *networks*, 137:119–126, 2021.

669 Alex Shtoff. torchcurves: Differentiable parametric curves in pytorch, 2025. URL <https://github.com/alexshft/torchcurves>.

672 Shriyank Somvanshi, Syed Aaqib Javed, Md Monzurul Islam, Diwas Pandit, and Subasish
 673 Das. A survey on kolmogorov-arnold network. *ACM Computing Surveys*, 2024.

674 Nitish Srivastava, Geoffrey Hinton, Alex Krizhevsky, Ilya Sutskever, and Ruslan Salakhutdinov.
 675 Dropout: a simple way to prevent neural networks from overfitting. *The journal of machine learning research*, 15(1):1929–1958, 2014.

678 Sidharth SS, Keerthana AR, Anas KP, et al. Chebyshev polynomial-based kolmogorov-arnold
 679 networks: An efficient architecture for nonlinear function approximation. *arXiv preprint*
 680 *arXiv:2405.07200*, 2024.

681 Justin M Turney, Andrew C Simmonett, Robert M Parrish, Edward G Hohenstein,
 682 Francesco A Evangelista, Justin T Fermann, Benjamin J Mintz, Lori A Burns, Jeremiah J
 683 Wilke, Micah L Abrams, et al. Psi4: an open-source ab initio electronic structure program.
 684 *Wiley Interdisciplinary Reviews: Computational Molecular Science*, 2(4):556–565, 2012.

685 Ashish Vaswani, Noam Shazeer, Niki Parmar, Jakob Uszkoreit, Llion Jones, Aidan N Gomez,
 686 Łukasz Kaiser, and Illia Polosukhin. Attention is all you need. *Advances in neural*
 687 *information processing systems*, 30, 2017.

689 Vasily Volkov and James W Demmel. Benchmarking gpus to tune dense linear algebra.
 690 In *SC'08: Proceedings of the 2008 ACM/IEEE conference on Supercomputing*, pp. 1–11.
 691 IEEE, 2008.

692 Stephen R Xie, Matthias Rupp, and Richard G Hennig. Ultra-fast interpretable machine-
 693 learning potentials. *npj Computational Materials*, 9(1):162, 2023.

695 Jinfeng Xu, Zheyu Chen, Jinze Li, Shuo Yang, Wei Wang, Xiping Hu, and Edith C-H
 696 Ngai. Fourierkan-gcf: Fourier kolmogorov-arnold network—an effective and efficient feature
 697 transformation for graph collaborative filtering. *arXiv preprint arXiv:2406.01034*, 2024.

698 Xingyi Yang and Xinchao Wang. Kolmogorov-arnold transformer. *arXiv preprint*
 699 *arXiv:2409.10594*, 2024.

701 Runpeng Yu, Weihao Yu, and Xinchao Wang. Kan or mlp: A fairer comparison. *arXiv*
 702 *preprint arXiv:2407.16674*, 2024.

702 Sangdoo Yun, Dongyoon Han, Seong Joon Oh, Sanghyuk Chun, Junsuk Choe, and Youngjoon
 703 Yoo. Cutmix: Regularization strategy to train strong classifiers with localizable features. In
 704 *Proceedings of the IEEE/CVF international conference on computer vision*, pp. 6023–6032,
 705 2019.

707 Xiaohua Zhai, Alexander Kolesnikov, Neil Houlsby, and Lucas Beyer. Scaling vision trans-
 708 formers. In *Proceedings of the IEEE/CVF conference on computer vision and pattern*
 709 *recognition*, pp. 12104–12113, 2022.

711 Hongyi Zhang, Moustapha Cisse, Yann N Dauphin, and David Lopez-Paz. mixup: Beyond
 712 empirical risk minimization. *arXiv preprint arXiv:1710.09412*, 2017.

715 Yaolong Zhang, Junfan Xia, and Bin Jiang. Physically motivated recursively embedded
 716 atom neural networks: incorporating local completeness and nonlocality. *Physical Review*
 717 *Letters*, 127(15):156002, 2021.

719 Jie Zhou, Ganqu Cui, Shengding Hu, Zhengyan Zhang, Cheng Yang, Zhiyuan Liu, Lifeng
 720 Wang, Changcheng Li, and Maosong Sun. Graph neural networks: A review of methods
 721 and applications. *AI open*, 1:57–81, 2020.

724 A LLM USAGE STATEMENT

726 We used LLMs for (i) polishing the text of the manuscript; (ii) finding related work and
 727 locating specific details in the corresponding papers; (iii) as a coding assistant during
 728 implementation of our codebase.

731 B MORE DETAILS ON FUNCTION PARAMETRIZATION

733 **The $\sigma(x)$ function** Section 3.1 of the main text describes the construction of the sigma
 734 grid used in the parametrization of all the functions lmKAN consists of. It involves any
 735 sigmoid-like function $\sigma(x)$, and, as was mentioned in the main text, our choice, which is
 736 given in Eq. 3 and is illustrated in Fig. 10, was motivated by computational efficiency.

$$739 \quad \sigma(x) = \begin{cases} 0.5 e^x, & x \leq 0, \\ 740 \quad 1 - 0.5 e^{-x}, & x > 0. \end{cases} \quad (3)$$

$$741 \quad \sigma(x)$$

$$742 \quad \sigma(x)$$

$$743 \quad \sigma(x)$$

$$744 \quad \sigma(x)$$

$$745 \quad \sigma(x)$$

$$746 \quad \sigma(x)$$

$$747 \quad \sigma(x)$$

$$748 \quad \sigma(x)$$

$$749 \quad \sigma(x)$$

$$750 \quad \sigma(x)$$

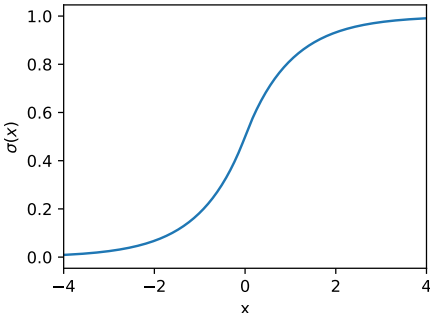
$$751 \quad \sigma(x)$$

$$752 \quad \sigma(x)$$

$$753 \quad \sigma(x)$$

$$754 \quad \sigma(x)$$

$$755 \quad \sigma(x)$$



751 Figure 10: The $\sigma(x)$ function defined in
 752 Eq. 3.

754 This construction is cheap to compute because the computational pipeline consists of a single
 755 exponential call and a few arithmetic operations, as elaborated in algorithm 1.

756 **Algorithm 1** Evaluation of $\sigma(x)$ with a single exponential call

757 **Input:** $x \in \mathbb{R}$
 758 **Output:** $\sigma(x)$
 759 1: $t \leftarrow \exp(-|x|)$ ▷ compute expensive exponential only once
 760 2: **if** $x > 0$ **then**
 761 3: $\sigma(x) \leftarrow 1 - 0.5t$
 762 4: **else**
 763 5: $\sigma(x) \leftarrow 0.5t$
 764 6: **end if**
 765 7: **return** $\sigma(x)$

766
 767 **Edge cases** Section 3.1 of the main text introduced sigma grids and the corresponding
 768 basis of second-order B-splines. For a grid with G intervals and $G - 1$ grid points, there
 769 are $G + 1$ basis functions, out of which $G - 1$ are given by second-order B-splines centered
 770 around all grid points, as illustrated in the right panel of Fig. 3 of the main text. The other
 771 two are given as linear functions on the leftmost and rightmost infinite intervals.
 772

773 The second-order B-splines given in the right panel of Fig. 3 are defined to linearly increase
 774 from 0 to 1 from the left grid point to the central one and then linearly decrease from 1 to 0
 775 from the central grid point to the right grid point. This construction is well-defined for all
 776 the inner grid points but requires additional definitions for the B-splines centered around
 777 the leftmost and rightmost grid points, as these do not have left and right neighboring grid
 778 points, respectively.

779 In order to define these edge B-splines, we introduce 'ghost' left and right grid points. The
 780 position of the left ghost point is given as $\mathcal{G}[0] - (\mathcal{G}[1] - \mathcal{G}[0])$, where $\mathcal{G}[0]$ and $\mathcal{G}[1]$ are the
 781 positions of leftmost and second leftmost grid points respectively. The right ghost point is
 782 defined similarly. With such a notation of additional grid points, we can define edge B-splines
 783 similarly to all the others.

784 Finally, there are two linear basis functions on the leftmost and rightmost infinite intervals.
 785 We define them to be 0-s in the leftmost and rightmost grid points, linearly increasing to
 786 1-s at the left and right ghost points and continuing to left and right infinities with the same
 787 slope, respectively.

788 **Direct σ -grid vs. uniform grid after pre-normalization by $\sigma(x)$** A natural question
 789 is how the proposed sigma grid construction differs from a simpler alternative that first maps
 790 the input via $x' = \sigma(x) \in (0, 1)$ and then fits a piecewise-linear function $g(x')$ on a uniform
 791 grid over $[0, 1]$.
 792

793 In general, the resulting functions in the original x -domain, $f(x)$ and $f'(x) = g(\sigma(x))$,
 794 are not identical. Most importantly, $f'(x)$ is no longer piecewise linear within each x -grid
 795 interval. The most notable discrepancy appears in the tails: $f'(x)$ has horizontal (constant)
 796 asymptotes when $x \rightarrow \pm\infty$, whereas $f(x)$ —by construction on the σ -grid—exhibits linear
 797 asymptotes.

798 Horizontal asymptotes entail vanishing gradients in the tails, a behavior widely implicated
 799 in training difficulties and one reason ReLU activations often outperform tanh (Glorot et al.,
 800 2011). For these reasons, we adopt the direct σ -grid parametrization in practice.

801
 802 **B.1 STANDALONE TWO-DIMENSIONAL FUNCTION COMPUTATION**

803
 804 Algorithm 2 provides a recipe to compute a standalone two-dimensional function given our
 805 parametrization scheme. See discussion in Sec. 3.1 of the main text.

806
 807 **C COMPUTATIONAL COST**

808
 809 Algorithm 3 represents a computational pipeline to compute the forward pass of an entire
 810 2D ImKAN layer.

810 **Algorithm 2** $\mathcal{O}(1)$ evaluation of a standalone 2D lmKAN function. Red lines indicate
 811 computations that can be reused when computing many 2D functions for the same arguments,
 812 while green lines indicate computations that have to be repeated for each 2D function.
 813

814 **Input:** scalars $x_1, x_2 \in \mathbb{R}$; grid points \mathbf{G} ; parameters $\mathbf{P} \in \mathbb{R}^{[G+1, G+1]}$

815 $\mathbf{P}[i_1, i_2]$ stores the function value on the (i_1, i_2) -th grid point

816 **Output:** output $y \in \mathbb{R}$

817 1: **function** **Eval2D**(x_1, x_2) \triangleright Handling of edge-interval cases described above is omitted
 818 for brevity.
 819 2: $i_1 \leftarrow \lfloor \sigma(x_1) G \rfloor$
 820 3: $i_2 \leftarrow \lfloor \sigma(x_2) G \rfloor$
 821 4: $B_{i_1 i_2}(x_1, x_2) \leftarrow \frac{\mathbf{G}[i_1 + 1] - x_1}{\mathbf{G}[i_1 + 1] - \mathbf{G}[i_1]} \frac{\mathbf{G}[i_2 + 1] - x_2}{\mathbf{G}[i_2 + 1] - \mathbf{G}[i_2]}$
 822 5: $B_{i_1+1 i_2}(x_1, x_2) \leftarrow \frac{x_1 - \mathbf{G}[i_1]}{\mathbf{G}[i_1 + 1] - \mathbf{G}[i_1]} \frac{\mathbf{G}[i_2 + 1] - x_2}{\mathbf{G}[i_2 + 1] - \mathbf{G}[i_2]}$
 823 6: $B_{i_1 i_2+1}(x_1, x_2) \leftarrow \frac{\mathbf{G}[i_1 + 1] - x_1}{\mathbf{G}[i_1 + 1] - \mathbf{G}[i_1]} \frac{x_2 - \mathbf{G}[i_2]}{\mathbf{G}[i_2 + 1] - \mathbf{G}[i_2]}$
 824 7: $B_{i_1+1 i_2+1}(x_1, x_2) \leftarrow \frac{x_1 - \mathbf{G}[i_1]}{\mathbf{G}[i_1 + 1] - \mathbf{G}[i_1]} \frac{x_2 - \mathbf{G}[i_2]}{\mathbf{G}[i_2 + 1] - \mathbf{G}[i_2]}$
 825 8: $y \leftarrow 0$
 826 9: $y += B_{i_1 i_2}(x_1, x_2) \mathbf{P}[i_1, i_2]$
 827 10: $y += B_{i_1+1 i_2}(x_1, x_2) \mathbf{P}[i_1+1, i_2]$
 828 11: $y += B_{i_1 i_2+1}(x_1, x_2) \mathbf{P}[i_1, i_2+1]$
 829 12: $y += B_{i_1+1 i_2+1}(x_1, x_2) \mathbf{P}[i_1+1, i_2+1]$
 830 13: **return** y
 831 14: **end function**

832 As the algorithm shows, the preamble part contributes only to an asymptotically insignificant
 833 $\mathcal{O}(N)$ term, where N is the input (N_{in}) or output (N_{out}) dimension. Given that the total
 834 number of 2D functions in an lmKAN layer is $[N_{\text{in}}/2]N_{\text{out}}$, the total number of required
 835 multiply-add operations for the dominant, $\mathcal{O}(N^2)$, part is $4[N_{\text{in}}/2]N_{\text{out}} = 2N_{\text{in}}N_{\text{out}}$, just $2\times$
 836 that of a linear layer of the same shape.

D HESSIAN REGULARIZATION

843 Direct fitting of splined functions with a fine grid imposes additional challenges related
 844 to generalization. The problem is illustrated in Fig. 11a for the simple case of fitting a
 845 standalone one-dimensional function parametrized by second-order B-splines on a uniform
 846 grid on $[0, 1]$ with $G = 40$ intervals, $f(x) = \sum_i p_i B_i(x)$.

847 Ground truth is an exact parabola, and the training set consists of 5 points, which are
 848 illustrated on the plot. Since the number of grid points is large, the model has enough
 849 flexibility to reproduce the training set exactly, but generalization is quite off. With such a
 850 fine grid, only a few B-splines, marked as bold on the bottom panel of Fig. 11a, take non-zero
 851 values for the training points. Thus, only the coefficients p_i associated with these active
 852 B-splines receive non-zero gradient during training, while all the others have no incentive to
 853 evolve from the random values assigned at initialization. Standard L2 regularization is not
 854 much better, as it simply pushes all non-active coefficients p_i to zero, which also results in a
 855 non-meaningful approximation after training.

856 When dealing with a similar problem, Xie et al. (2023) employed off-diagonal regularization
 857 based on a finite-difference scheme for the second derivative. One can put regularization
 858 terms as $\lambda \sum_i (p_i - p_{i+1})^2$ for first derivative, $\lambda \sum_i (p_i - 2p_{i+1} + p_{i+2})^2$ for second, and so on.
 859 Such regularization schemes result in meaningful approximations after training, as illustrated
 860 in Fig. 11b.

864 **Algorithm 3** Forward pass of a 2D lmKAN layer.
865

866 **Input:** input vector $\mathbf{x} \in \mathbb{R}^{N_{\text{in}}}$, parameter tensor $\mathbf{P} \in \mathbb{R}^{[G+1, G+1, N_{\text{in}}/2, N_{\text{out}}]}$.
867 $\mathbf{P}[i_1, i_2, \text{input_index}, \text{output_index}]$ is the value of $f_{\text{input_index}, \text{output_index}}$ at the
868 i_1-, i_2- th grid point.
869 **Output:** output vector $\mathbf{y} \in \mathbb{R}^{N_{\text{out}}}$

870 1: $\mathbf{y} \leftarrow \mathbf{0}$
871 2: **for** $\text{input_index} = 0$ **to** $N_{\text{in}}/2 - 1$ **do**
872 3: $i_1, i_2, B_{i_1 i_2}(x_1, x_2), B_{i_1+1 i_2}(x_1, x_2), B_{i_1 i_2+1}(x_1, x_2), B_{i_1+1 i_2+1}(x_1, x_2) \leftarrow$
873 **Preamble**($\mathbf{x}[2 \cdot \text{input_index}], \mathbf{x}[2 \cdot \text{input_index} + 1]$)
874 4: **for** $\text{output_index} = 0$ **to** $N_{\text{out}} - 1$ **do**
875 5: $\mathbf{y}[\text{output_index}] += B_{i_1 i_2}(x_1, x_2) \mathbf{P}[i_1, i_2, \text{input_index}, \text{output_index}]$
876 6: $\mathbf{y}[\text{output_index}] += B_{i_1+1 i_2}(x_1, x_2) \mathbf{P}[i_1+1, i_2, \text{input_index}, \text{output_index}]$
877 7: $\mathbf{y}[\text{output_index}] += B_{i_1 i_2+1}(x_1, x_2) \mathbf{P}[i_1, i_2+1, \text{input_index}, \text{output_index}]$
878 8: $\mathbf{y}[\text{output_index}] += B_{i_1+1 i_2+1}(x_1, x_2) \mathbf{P}[i_1+1, i_2+1, \text{input_index}, \text{output_index}]$
879 9: **end for**
880 10: **end for**

881 11: **function** **Preamble**(x_1, x_2) \triangleright Handling of edge-interval cases is omitted for brevity.
882 See Appendix B for more details.
883 **Input:** x_1, x_2 ; precomputed grid points \mathcal{G} ;
884 precomputed inverse areas $\mathbf{A}_{\text{inv}}[i_1, i_2] = [(\mathcal{G}[i_1 + 1] - \mathcal{G}[i_1])(\mathcal{G}[i_2 + 1] - \mathcal{G}[i_2])]^{-1}$
885 **Output:** indices i_1, i_2 and
886 B-splines $B_{i_1 i_2}(x_1, x_2), B_{i_1+1 i_2}(x_1, x_2), B_{i_1 i_2+1}(x_1, x_2), B_{i_1+1 i_2+1}(x_1, x_2)$
887 12: $i_1 \leftarrow \lfloor \sigma(x_1) G \rfloor$
888 13: $i_2 \leftarrow \lfloor \sigma(x_2) G \rfloor$
889 14: $B_{i_1 i_2}(x_1, x_2) \leftarrow (\mathcal{G}[i_1 + 1] - x_1)(\mathcal{G}[i_2 + 1] - x_2) \mathbf{A}_{\text{inv}}[i_1, i_2]$
890 15: $B_{i_1+1 i_2}(x_1, x_2) \leftarrow (x_1 - \mathcal{G}[i_1])(\mathcal{G}[i_2 + 1] - x_2) \mathbf{A}_{\text{inv}}[i_1, i_2]$
891 16: $B_{i_1 i_2+1}(x_1, x_2) \leftarrow (\mathcal{G}[i_1 + 1] - x_1)(x_2 - \mathcal{G}[i_2]) \mathbf{A}_{\text{inv}}[i_1, i_2]$
892 17: $B_{i_1+1 i_2+1}(x_1, x_2) \leftarrow (x_1 - \mathcal{G}[i_1])(x_2 - \mathcal{G}[i_2]) \mathbf{A}_{\text{inv}}[i_1, i_2]$
893 18: **return** $i_1, i_2, B_{i_1 i_2}(x_1, x_2), B_{i_1+1 i_2}(x_1, x_2), B_{i_1 i_2+1}(x_1, x_2), B_{i_1+1 i_2+1}(x_1, x_2)$
894 19: **end function**

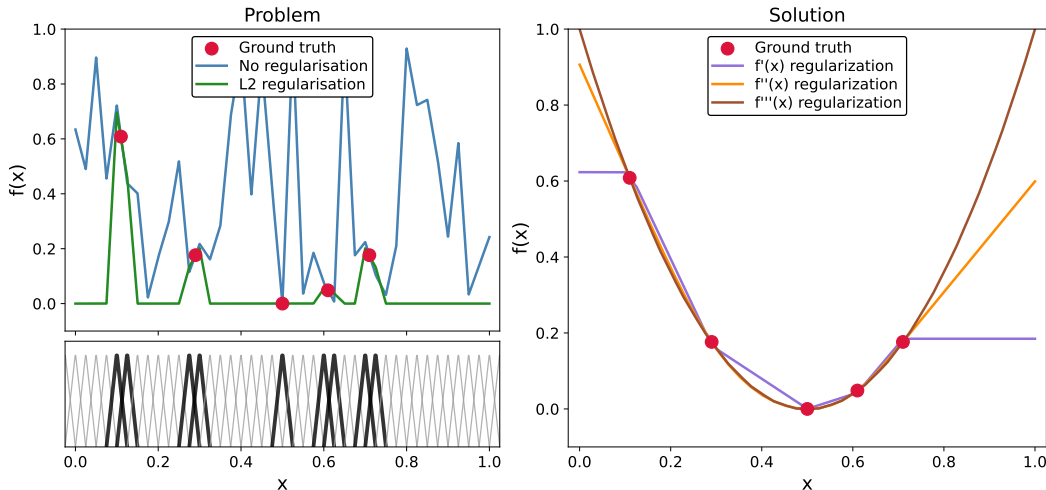


Figure 11: Generalization pitfall.

913 We implemented CUDA kernels for 2D lmKANs, which express general high-dimensional
914 mapping in terms of building blocks of two-dimensional functions. For 2D functions, we
915 use off-diagonal regularization based on the squared Frobenius norm of the Hessian, a

918 rotationally invariant measure of curvature in any direction, which is not to be confused
 919 with the Laplacian. Furthermore, our finite-difference schemes take into account that the
 920 grids, introduced in Sec. 3.1, are not uniform. The exact formulas are given below.

921 The Hessian of a function is zero if and only if the function is linear. Therefore, the use of
 922 a very strong Hessian-based regularization leads to linearization of the trained functions,
 923 enforcing them to converge to $f(x_1, x_2) = ax_1 + bx_2 + c$. This makes the whole lmKAN
 924 equivalent to an MLP of the same shape, modulo training dynamics. In other words, the
 925 Hessian regularization coefficient λ can be used to smoothly adjust the lmKAN behavior
 926 between fully unconstrained lmKAN and MLP extremes. This observation that lmKANs
 927 with heavy Hessian regularization match non-regularized MLPs suggests that one should
 928 use a combination of the proposed regularization scheme with standard ones, such as L2 or
 929 dropout (Srivastava et al., 2014), for the best results.

930 D.1 DETAILED FORMULATION OF THE HESSIAN REGULARIZATION

931 We use the following finite-differences approximation for the second derivative with respect
 932 to x_1 :

$$936 \frac{\partial^2 f}{\partial x_1^2} \bigg|_{(x_1, x_2)} \approx \frac{2(h_\ell f(x_1 + h_r, x_2) - (h_\ell + h_r) f(x_1, x_2) + h_r f(x_1 - h_\ell, x_2))}{h_\ell h_r (h_\ell + h_r)}, \quad (4)$$

938 where h_ℓ is the spacing between left and central grid points, while h_r is the spacing between
 939 central and right grid points. The corresponding expression in terms of the coefficients $p_{i,j}$
 940 is given as:

$$942 D_{x_1, x_1; i, j} = \frac{2(h_i p_{i+1, j} - (h_i + h_{i+1}) p_{i, j} + h_{i+1} p_{i-1, j})}{h_i h_{i+1} (h_i + h_{i+1})} \quad (5)$$

945 For the second derivative with respect to x_2 we use an analogous expression:

$$948 \frac{\partial^2 f}{\partial x_2^2} \bigg|_{(x_1, x_2)} \approx \frac{2(h_b f(x_1, x_2 + h_u) - (h_b + h_u) f(x_1, x_2) + h_u f(x_1, x_2 - h_b))}{h_b h_u (h_b + h_u)}, \quad (6)$$

951 where h_u and h_b are upper and bottom spacings, respectively.

$$952 D_{x_2, x_2; i, j} = \frac{2(h_j p_{i, j+1} - (h_j + h_{j+1}) p_{i, j} + h_{j+1} p_{i, j-1})}{h_j h_{j+1} (h_j + h_{j+1})} \quad (7)$$

955 For the mixed derivative our finite-differences scheme is the following:

$$957 \frac{\partial^2 f}{\partial x_1 \partial x_2} \bigg|_{(x_1, x_2)} \approx \\ 958 f(x_1 + h_r, x_2 + h_p) - f(x_1 + h_r, x_2 - h_b) - f(x_1 - h_l, x_2 + h_p) + f(x_1 - h_l, x_2 - h_b) \\ 959 \quad (h_r + h_l) (h_p + h_b) \quad (8)$$

$$963 D_{x_1, x_2; i, j} = \frac{p_{i+1, j+1} - p_{i+1, j-1} - p_{i-1, j+1} + p_{i-1, j-1}}{(h_i + h_{i+1}) (h_j + h_{j+1})} \quad (9)$$

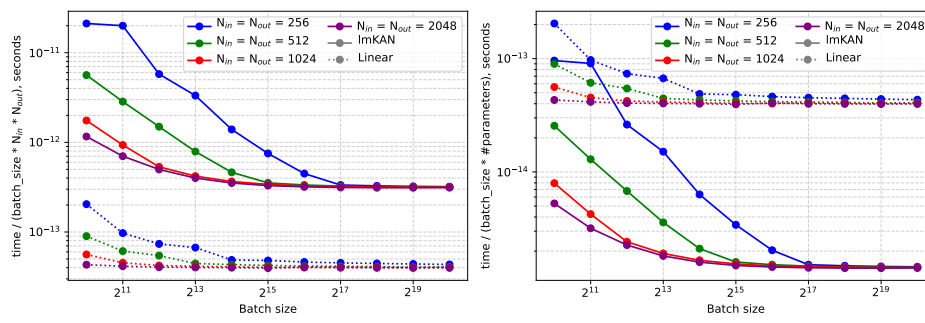
965 The final regularization term is the following:

$$968 H_{i, j} = D_{x_1, x_1; i, j}^2 + 2D_{x_1, x_2; i, j}^2 + D_{x_2, x_2; i, j}^2. \quad (10)$$

970 In order to compute the total regularization term for the whole model, we 1) average $H_{i, j}$
 971 across all the grid points and 2) sum these values across all the 2D functions within all the
 lmKAN layers in the model.

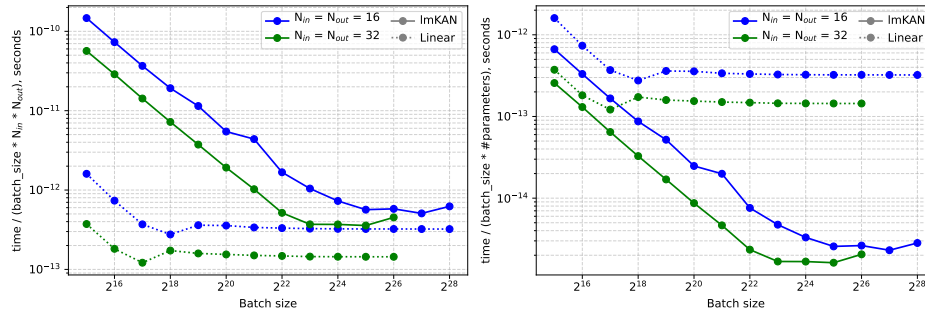
972 E CUDA KERNELS
973
974

975 The performance of our CUDA kernels with 16x16 tile size in the limit of large dimensions
976 is summarized in Fig. 12. All the lmKAN curves are computed with the largest number of
977 grid intervals $G = 20$ available for the 16x16 tile size. We compare the inference efficiency of
978 lmKAN and linear layers. On the left panel, we normalize time by the shape of the layers.
979 Fig. 12 illustrates a clear convergence of these normalized times to the same value for all the
980 dimensions. In the limit of large batch sizes, the forward pass of an lmKAN layer is $\sim 8 \times$
981 slower compared to a linear layer with the same shape. At the same time, an lmKAN layer
982 contains a significantly larger number of parameters than a linear layer of the same shape.
983 Thus, inference time per parameter is significantly better for lmKAN layers, about 27 times,
984 as illustrated on the right panel of Fig. 12.



997 Figure 12: The performance of our CUDA kernels on the H100 SXM GPU in comparison
998 with the linear layer in the limit of large dimensions. Left panel - time normalized by shape.
999 Right panel - time normalized by the number of parameters.

1000
1001
1002 Fig. 13 is an analogous illustration but for small dimensions - 16 and 32. Our CUDA kernels
1003 are better adjusted for such small dimensions, and thus, relative performance compared to
1004 linear layers is even higher in this case.
1005
1006
1007



1018 Figure 13: The performance of our CUDA kernels on the H100 SXM GPU in comparison
1019 with the linear layer for small dimensions. Left panel - time normalized by shape. Right
1020 panel - time normalized by the number of parameters.

1024 Finally, Fig. 14 illustrates the inference efficiency depending on the number of grid intervals
1025 G , which control the number of parameters. The time indeed does not depend on G in the
large batch size limit.

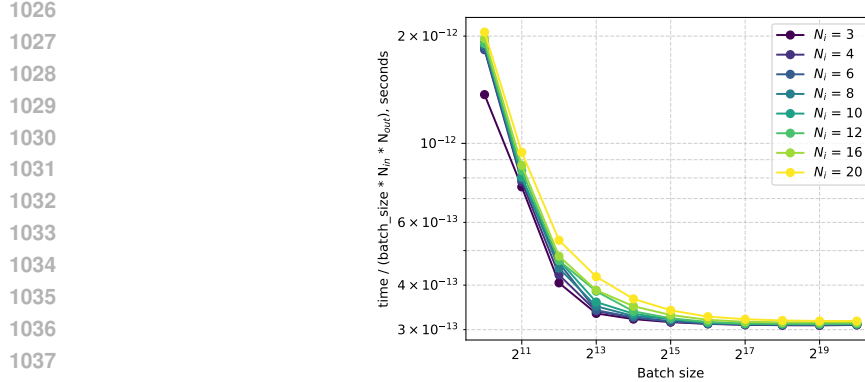


Figure 14: Inference efficiency of an lmKAN layer depending on the number of grid intervals G .

F PRECONDITIONING AND FITTING SCHEME

The first thing we attempted upon implementing the CUDA kernels was to fit a model with the highest grid resolution, $G = 40$, supported for the 8×8 tile on the H100 GPU. In this setup, each 2D function had as many as $41^2 = 1681$ trainable parameters. We found that the training was unstable, so we designed a preconditioning and multi-stage fitting pipeline to stabilize it. We employed this pipeline consistently for all our experiments.

The subsequent evidence revealed that lmKANs (similarly to KANs, as Sec. 4.4 illustrates) are progressively harder to fit as grid resolution increases. In other words, our very first experiment was the most challenging one. At more moderate grid resolutions, preconditioning measures can likely be simplified, if not omitted altogether. Specifically, we think that a fitting scheme omitting additional preconditioning terms, but preserving the Hessian regularization decay phase, which is described in the following, could be effective. With that, below is the description of the current pipeline.

F.1 PRECONDITIONING

We precondition lmKAN layers by adding linear terms into the overall functional form. We use one of the following:

$$y = \gamma \text{ lmKAN}(x) + \text{ReLU}(\text{Linear}(x)) \quad (11a)$$

$$y = \gamma \text{ lmKAN}(x) + \text{Linear}(\text{ReLU}(x)) \quad (11b)$$

where the lmKAN weight, γ , is first set to 0 and then is gradually increased in our multistaged fitting procedure described later. In the case of ReLU-last preconditioning of Eq. 11a, we insert ReLU into all the layers except the last one; for ReLU-first preconditioning of Eq. 11b, we insert ReLU into all the layers except the first one. Therefore, at the beginning, when the lmKAN weight is zero, the model is equivalent to a pure MLP-based one for both types of preconditioning.

A merit of ReLU-first preconditioning is that during inference the whole Eq. 11b can be absorbed into a single lmKAN layer whenever the number of grid intervals G is even, that is, when the origin is one of the grid points, see more details in Appendix G.1. Thus, this type of preconditioning does not increase inference cost in any way. This is an advantage over the original KAN preconditioning scheme (Liu et al., 2024), which requires the additional computation of the computationally expensive transcendental function SiLU for each edge at inference.

1080 Because of the possibility of such an absorption, the total inference FLOPs of a ReLU-first
 1081 preconditioned lmKAN layer are $2\times$ those of a linear layer of the same shape, while for the
 1082 ReLU-last preconditioning, the slowdown factor is $3\times$, taking into account the linear branch.
 1083

1084 F.2 FITTING PROCEDURE 1085

1086 Our fitting scheme consists of several phases:

1087 **Phase I - pure MLP:** γ is set to 0, so the whole architecture is operating in pure MLP
 1088 mode. This part is typically very short.

1089 **Phase II - turning on lmKAN:** γ is linearly (over time) increased from 0 to 0.3. After
 1090 that, there is some part with the constant $\gamma = 0.3$. At this phase, we use very strong (=
 1091 with very high coefficient λ) Hessian regularization introduced in Appendix D. For all the
 1092 subsequent phases, lmKAN weight γ is fixed at 0.3. The pipeline is also stable if increasing
 1093 γ to 1.0, but in a few, though non-systematic, experiments, we found that using 0.3 value
 1094 leads to slightly better final accuracy.

1095 **Phase III - Hessian regularization decay:** At this phase, we gradually decay the
 1096 strength of the Hessian regularization λ from the initial very high value to the target value
 1097 if this regularization is intended to be utilized in this fitting procedure and to nearly zero
 1098 otherwise.

1099 **Phase IV - Main lmKAN fitting part:** In this final phase, we keep Hessian regularization
 1100 constant at the value reached in the previous phase. The model is fit with the given learning
 1101 rate schedule. In the experiments in this work, we use a constant learning rate for the most
 1102 part of this phase, and step or exponential learning rate decay at the end.

1103 An example of the described fitting procedure for one of the training runs we did for numerical
 1104 experiments described in Sec. 4.1 of the main text and in the Appendix G.2 is given in
 1105 Fig. 15.

1106 F.3 COMPARISON OF THE PRECONDITIONING SCHEMES 1107

1108 We fitted lmKAN models with both types of preconditioning for the CIFAR-10 dataset and
 1109 for general function approximation. The results are given in Fig. 16 and Fig. 17. Overall,
 1110 the ReLU-last type of preconditioning appeared to lead to slightly more accurate models,
 1111 but this small gain in accuracy does not justify additional computational cost.

1112 When designing some of our experiments we did not know this yet. Therefore, some of them
 1113 use the ReLU-last type of preconditioning.

1114 We use the ReLU-last type of preconditioning for Figures 21, 22, 23, and 24. We use the
 1115 ReLU-first type of preconditioning for Figures 5, 8, 9, 26, and 27.

1116 In other words, the performance of lmKANs on the methane datasets can likely be further
 1117 improved by switching from the ReLU-last type of preconditioning to the ReLU-first one.
 1118 However, since the observed gains in efficiency are already more than an order of magnitude
 1119 in terms of the H100 wall-clock time, we left this for future work.

1121 G EXPERIMENTS 1122

1124 G.1 GENERAL DETAILS ABOUT THE BENCHMARKING PROTOCOLS 1125

1126 Within the scope of this work, we primarily focus on the saturated throughput in the limit
 1127 of large batch sizes. Thus, we benchmark all the models for progressively large batch sizes
 1128 until reaching saturation. All the models are benchmarked with **10** warm-up dry runs, and
 1129 **20** timed runs. Overall, we tried to optimize each model as much as possible while staying
 1130 within the limits of full precision `float32` data type.

1131 MLPs employed in this work consist of three types of layers - linear ones, ReLU activations,
 1132 and batch normalizations. At inference, batch normalizations simply perform elementwise
 1133 linear transformation and thus can be absorbed into the weights of linear layers. We perform
 this operation manually and, on top of that, compile the model with the `torch_tensorrt`

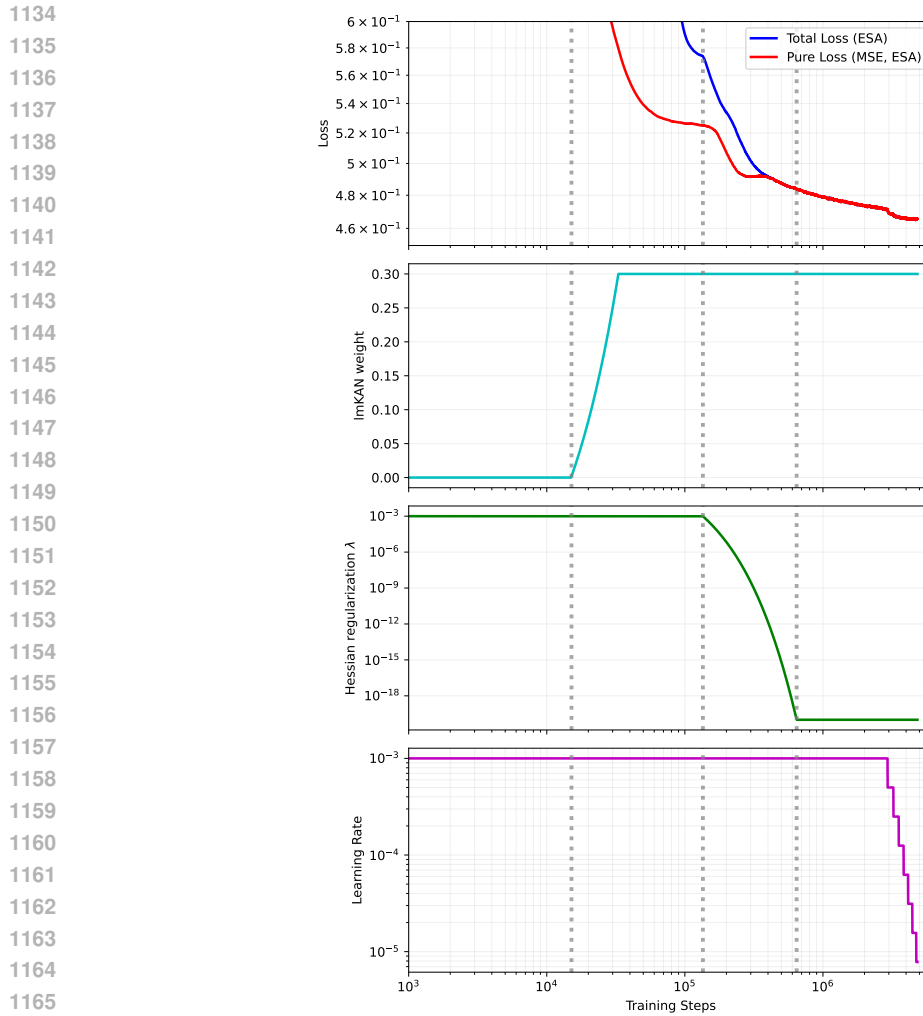


Figure 15: The multi-stage fitting procedure we use. Total loss indicates the full loss, including the Hessian regularization term. Pure loss is only the MSE part. For clarity, we plot exponential moving averages of losses. Note that the horizontal scale is logarithmic. If it is linear, the first couple of phases are hard to discern as they are very short. The fourth phase takes most of the training budget. This training run corresponds to the unregularized lmKAN, where Hessian regularization is turned on only at the beginning of the fitting to ensure stability. At the end of phase III, it reaches a nearly zero value, which, in this case, is 10^{-20} .

backend (with `tf32` disabled to ensure full precision `float32`). We use the same compilation strategy for FastKANs.

For lmKANs, when using ReLU-first preconditioning (see more details in Appendix F), we absorb the entire expression in Eq. 11b into the weights of the lmKAN layer. This modification requires updating the lmKAN 2D functions as $f(x_1, x_2) \leftarrow \gamma f(x_1, x_2) + w_1 \text{ReLU}(x_1) + w_2 \text{ReLU}(x_2)$. Our construction allows for doing this absorption exactly whenever the origin is one of the grid points, which, in turn, is the case when the number of grid intervals G is even. On top of that, batch normalizations are absorbed similarly to MLPs. We do not compile lmKAN models.

For lmKAN models with the ReLU-last preconditioning we absorb only the lmKAN weight γ .

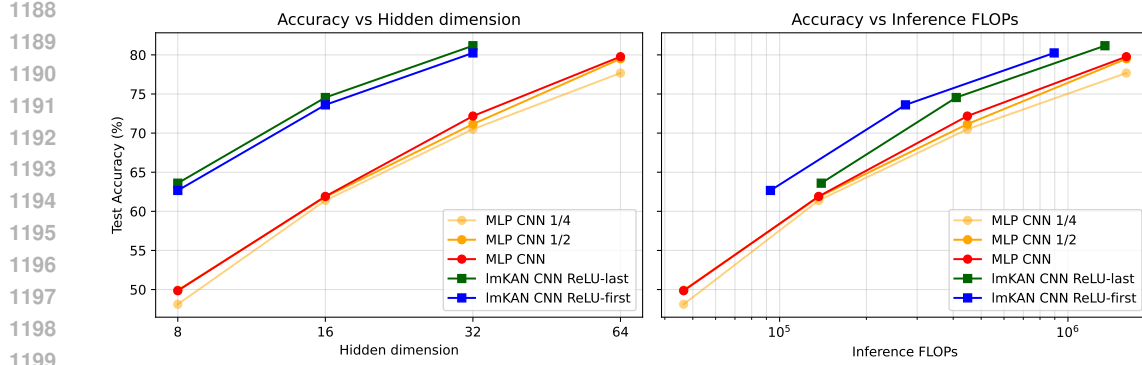


Figure 16: Comparison of the preconditioning schemes when fitting lmKANs on the CIFAR-10 dataset.

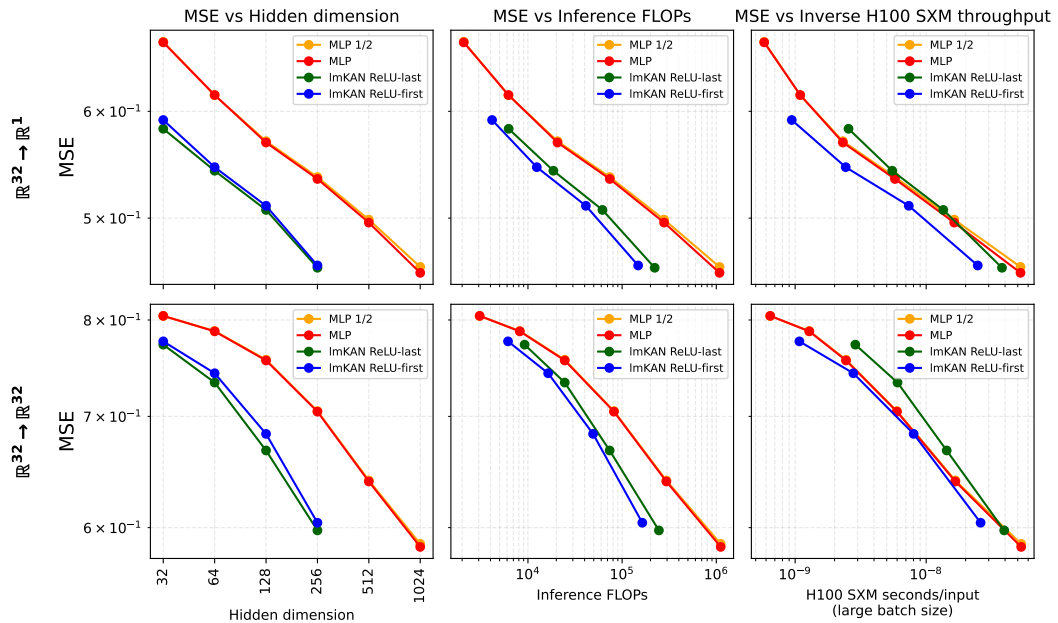


Figure 17: Comparison of the preconditioning schemes when fitting lmKANs within general function approximation setup.

G.2 GENERAL FUNCTION APPROXIMATION

Both MLPs and lmKANs use batch normalizations. We set `affine=True` for MLPs as it is the standard choice, and `affine=False` for lmKANs in accordance with sigma grids introduced in Sec. 3.1. MLPs use ReLU activations, while lmKANs do not require any additional activation functions. We use $G = 12$ for all the lmKAN models, as this was the optimal value found in the ablation study described below. Pseudocode for both models is available in Fig. 18. Both students have two hidden layers, which is one more than both Cybenko (Cybenko, 1989) (the one for MLPs) and Kolmogorov-Arnold universal approximation theorems require. This setup, however, is more realistic, as MLPs with exactly one hidden layer are rarely used in practice.

```

1242 MLP student
1243
1244 Linear(input_dim → hidden_dim)
1245 BatchNorm1d(hidden_dim, affine=True)
1246 ReLU()
1247 Linear(hidden_dim → hidden_dim)
1248 BatchNorm1d(hidden_dim, affine=True)
1249 ReLU()
1250 Linear(hidden_dim → output_dim)
1251
1252
1253
1254 lmKAN student
1255 lmKANLayer(input_dim → hidden_dim)
1256 BatchNorm1d(hidden_dim, affine=False)
1257 lmKANLayer(hidden_dim → hidden_dim)
1258 BatchNorm1d(hidden_dim, affine=False)
1259 lmKANLayer(hidden_dim → output_dim)
1260
1261
1262
1263
1264
1265
1266
1267
1268
1269
1270
1271
1272
1273
1274
1275
1276
1277
1278
1279
1280
1281
1282
1283
1284
1285
1286
1287
1288
1289
1290
1291
1292
1293
1294
1295

```

Figure 18: Pseudo code for MLP and lmKAN students.

The performance of lmKANs when approximating a $\mathbb{R}^{32} \rightarrow \mathbb{R}^{32}$ function generated similarly as the $\mathbb{R}^{32} \rightarrow \mathbb{R}^1$ described in the main text is given in Fig. 19.

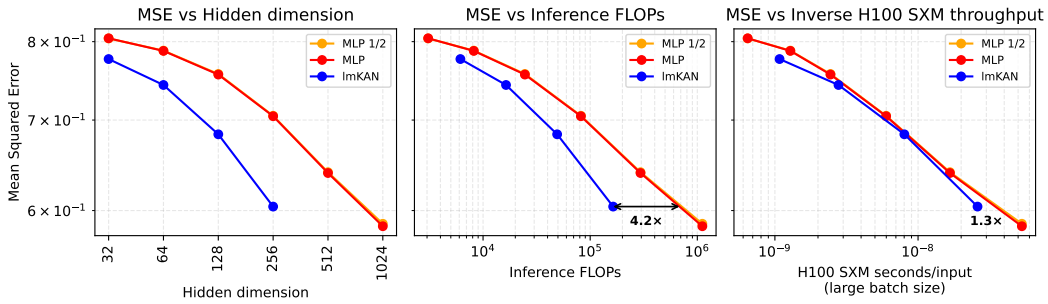
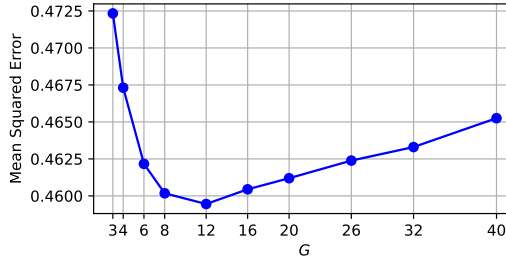
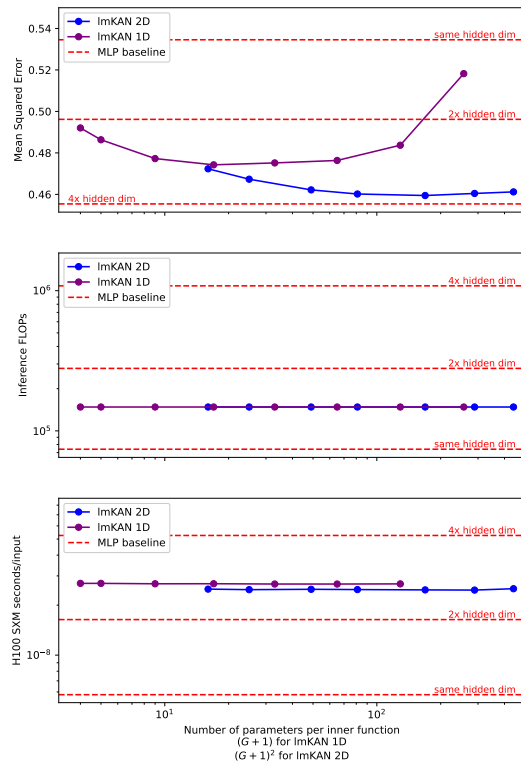


Figure 19: lmKAN vs MLP for general, $\mathbb{R}^{32} \rightarrow \mathbb{R}^{32}$, function approximation. The "MLP 1/2" line corresponds to the outcome of the fitting procedure with only half of the training steps compared to the "MLP" one.

There is a trend that the relative performance of lmKANs improves with the scale. It is clearly seen on the MSE vs FLOPs panel. On the MSE vs H100 wall-clock time panel, it is first masked by the non-homogeneous efficiency of the code, but next still reveals itself for the largest hidden dimensions.

We investigate the effect of the chosen number of grid intervals G on the resulting lmKAN accuracy when approximating the $\mathbb{R}^{32} \rightarrow \mathbb{R}^1$ function with $\text{hidden_dim} = 256$. The result is given in Fig. 21.

Figure 20: Final MSE vs G for the $\text{hidden_dim}=256$ lmKAN model.

1296 G.3 PLOT WITH SHARED AXIS FOR THE NUMBER OF PARAMETERS PER EACH INNER
1297 FUNCTION
1298
1299
1300
13011327 Figure 21: The same plot as Fig. 4 of the main text, but in vertical format and with the
1328 shared x axis.
1329
1330
13311332 G.4 METHANE
1333
1334

Tabular datasets are the natural choice for feedforward fully connected neural networks. Popular tabular datasets, such as the Titanic (Kaggle) or housing prices (Harrison Jr & Rubinfeld, 1978), however, are not particularly convenient for this purpose. First, they are typically stochastic in nature - for instance, while it is possible to improve a guess on the survival based on the data available for the Titanic dataset, it is impossible to say for sure. Thus, even an arbitrarily large model fitted on arbitrarily many data points would have a non-zero limitation on the accuracy. In other words, the performance of a model translates into an error metric not so directly, making the comparisons between different models less illustrative. Second, these datasets are typically relatively small, making it challenging to sweep across a wide range of model scales to obtain a comprehensive picture of performance.

Machine learning models fit on such datasets belong to the class of so-called machine learning interatomic potentials (Behler & Parrinello, 2007; Bartók et al., 2010). This dataset is sufficiently large for the comparisons, containing more than seven million configurations. Additionally, this dataset is deterministic - the geometry of the corresponding methane configuration completely determines the target (formally, there can be a stochastic term due to the lack of complete convergence of ab initio computations for the quantum-mechanical energy, but it is negligible in practice).

1350

1351

Table 1: Summary of methane representations

1352

1353

1354

1355

1356

1357

1358

1359

1360

1361

1362

1363

1364

1365

1366

1367

1368

1369 The target, the potential energy of the system, is invariant with respect to rotations and
 1370 permutations of identical atoms³. Therefore, there are several viable representations of the
 1371 methane molecules depending on how these symmetries are addressed:

1372 **Cartesian Components:** The simplest representation is just a collection of all the Cartesian
 1373 components of all displacement vectors from the carbon atom to all the hydrogen atoms.
 1374 Since each methane molecule contains 4 hydrogen atoms, the total number of displacement
 1375 vectors is 4, and the total number of components is 12. When using this representation, we
 1376 simply concatenate all these components together and feed them to a fully connected MLP
 1377 or lmKAN whose input dimension is 12. This representation is not invariant with respect
 1378 to both rotations and permutations; thus, we use the corresponding augmentations during
 1379 training. We randomly permute hydrogen atoms and rotate each molecule whenever we
 1380 sample a minibatch from the training subset for each step of stochastic gradient descent.

1381 **Distances:** Another possible representation is a collection of all the interatomic distances
 1382 between all the atoms. Since the total number of atoms is 5, the number of all the interatomic
 1383 distances is $5 * 4 / 2 = 10$. Therefore, the input dimension of fully connected networks applied
 1384 to this representation is 10. This representation is invariant with respect to rotations but not
 1385 with respect to permutations. During training, we use only permutational augmentations.

1386

1387

1388

1389

1390

1391

1392

1393

1394

1395

1396

1397

1398

1399

1400

1401

1402 ³Formally, there is an additional symmetry, inversion, but the corresponding group contains only
 1403 two elements, thus it does not make much sense to treat it separately. We unite it with the group of
 rotations, and in the following, by rotation we mean proper or improper rotation.

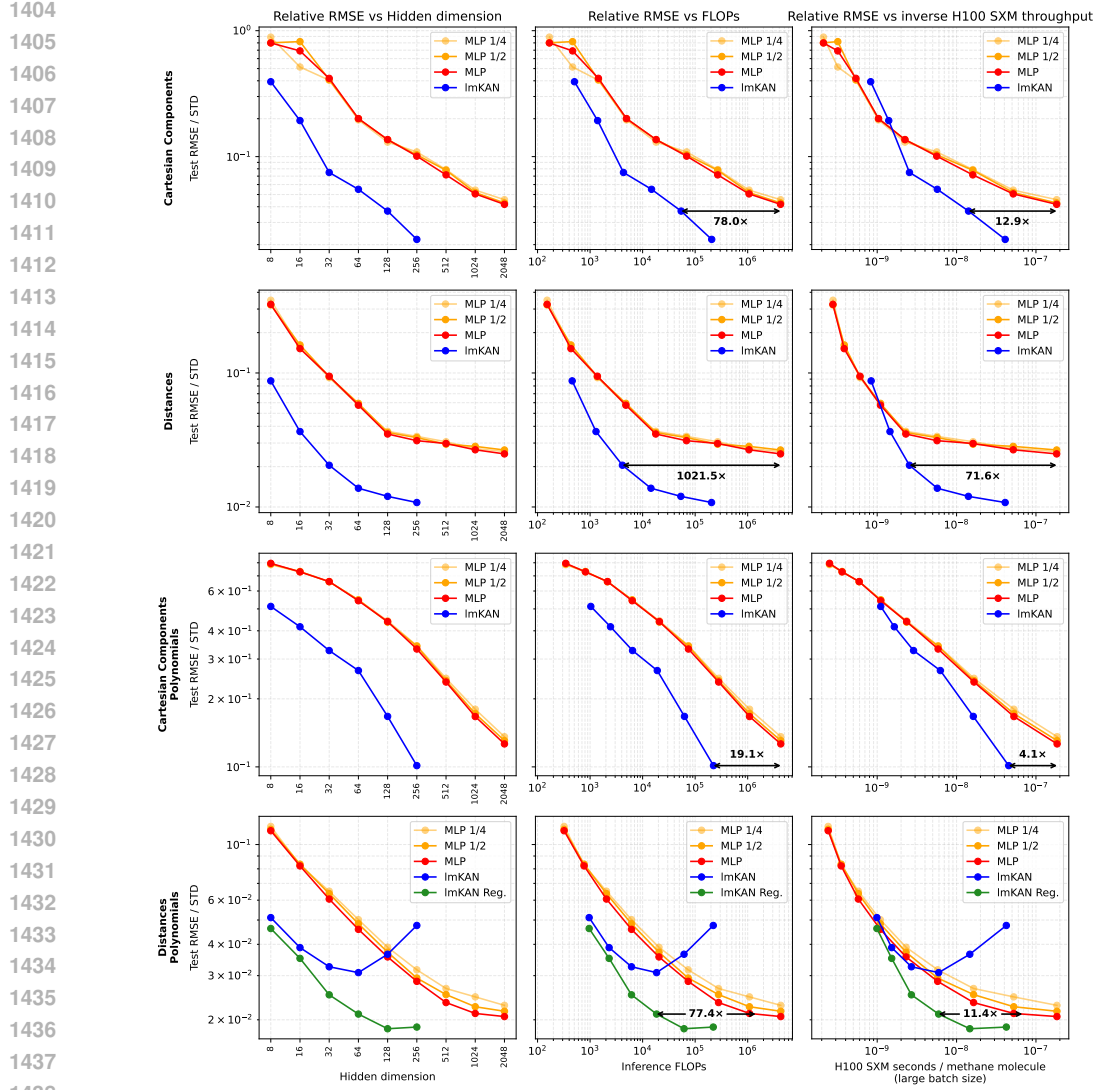


Figure 22: ImKAN vs MLP on the dataset of randomly displaced methane configurations. "ImKAN Reg." curve corresponds to ImKAN fitted with Hessian regularization introduced in Appendix D. On the vertical axis, we plot the relative Root Mean Squared Error, which is given as test RMSE normalized by the standard deviation of the target in the dataset. The "MLP 1/2" and "MLP 1/4" curves correspond to outcomes of fitting procedures with half and a quarter of the training budget, respectively.

Cartesian Components Polynomials: We compute power sum symmetric polynomials on top of the Cartesian components of the displacement vectors: $P_{\alpha_x, \alpha_y, \alpha_z} = \sum_{i=1}^{i=4} x_i^{\alpha_x} y_i^{\alpha_y} z_i^{\alpha_z}$ for non-negative integer $\alpha_x + \alpha_y + \alpha_z \leq 4$. The total number of such symmetric polynomials is 34 (excluding trivial $P_{0,0,0}$). This representation is invariant with respect to permutations but not with respect to rotations. Thus, during training we use only rotational augmentations.

Distances Polynomials: The final representation is a collection of non-trivial symmetric polynomials on top of the interatomic distances, constructed similarly to Allen et al. (2021). The total number of such polynomials is 31, and their exact formulas are given in Appendix G.4. This representation is invariant with respect to both rotations and permutations. Thus, we do not use any augmentations during training for this representation.

The described representations are summarized in Table 1. We systematically evaluate all four possible combinations of how the rotational and permutational symmetries can be

1458 incorporated into the fitting pipeline. Within the `Distances Polynomials` representation,
 1459 the methane dataset is tabular in the classical sense — it is a table with about 7.7 million
 1460 rows and 31 columns. For other representations, the dataset is tabular-like given the available
 1461 augmentation strategies. We randomly split the data into 7000000, 300000, and 432488
 1462 train, validation, and test molecules, respectively.

1463 For each representation, we fit the same families of MLP and lmKAN models as in the
 1464 previous section. The result is given in Fig. 22. For this dataset, we use $G = 28$, the optimal
 1465 value we found in ablation studies. Similarly to the previous experiment, we demonstrate
 1466 tight convergence of the baseline MLP models by providing three lines corresponding
 1467 to full, half, and quarter of the training budget, respectively. Overall, when compared
 1468 to domain-specific architectures, typically given by GNNs (Zhang et al., 2021) and/or
 1469 transformers (Pozdnyakov & Ceriotti, 2023), the introduced feedforward fully connected
 1470 models occupy a non-overlapping part of the Pareto frontier — they are less accurate, but
 1471 also orders of magnitude faster.

1472 The figure illustrates that lmKANs consistently outperform MLPs across all modalities.
 1473 Furthermore, the performance improvement is much larger compared to our previous ex-
 1474 periment. At the same accuracy level, lmKANs require up to many dozen times (or even
 1475 more for the `Distances` modality) less inference FLOPs, which results in **more than a 10 \times**
 1476 improvement of the inference H100 wall-clock time.

1477 Furthermore, Fig. 22 provides early indications that lmKANs sometimes can be more accurate
 1478 in the limit of large scale, that is, to have better generalizability. The second row of the
 1479 figure, corresponding to the `Distances` modality, illustrates that the rate of improvement of
 1480 MLP models becomes very slow, and it is questionable if this family of models would ever
 1481 surpass the accuracy achieved by lmKAN models at any scale.

1482 On the other hand, depending on the nature of the data, raw lmKANs, without the Hessian
 1483 regularization we proposed in Appendix D, can be more prone to overfitting. This happens for
 1484 the `Distances Polynomials` modality as the last row of Fig. 22 illustrates. This modality
 1485 incorporates all the symmetries into the representation and does not involve any sort
 1486 of augmentations. Therefore, it is likely that the generalization problem we outlined in
 1487 Appendix D takes place for this fitting setup. As the green line of the fourth row of Fig. 22
 1488 illustrates, the Hessian regularization is sufficient to overcome the overfitting. Properly
 1489 regularized lmKANs were found to outperform the MLPs and be Pareto-optimal from the
 1490 point of view of both inference FLOPs and inference H100 wall-clock time.

1491

1492

1493

G.4.1 ABLATIONS

1494

1495

1496 The ablation study on the effect of Hessian regularization is given in Fig. 23, and the effect
 1497 of the number of grid intervals G in Fig. 24.

1498

1499

1500

1501

1502

1503

1504

1505

1506

1507

1508

1509

1510

1511

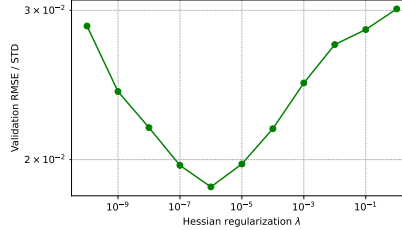
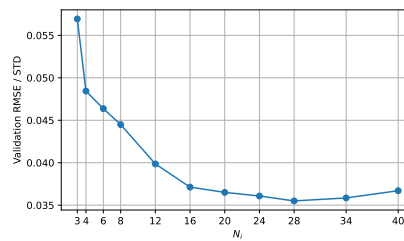


Figure 23: Effect of the strength of Hessian regularization on the validation error when fitting lmKAN with `hidden_dim = 256` on the methane dataset using the `Distances Polynomials` representation.

1512
1513
1514
1515
1516
1517
1518
1519
1520



1521 Figure 24: Effect of the number of grid intervals G on the validation error when fitting
1522 lmKAN with `hidden_dim` = 128 on the methane dataset using the Cartesian Components
1523 representation.

1524
1525
1526
1527
1528
1529
1530
1531
1532
1533
1534
1535
1536
1537
1538
1539
1540
1541
1542
1543
1544
1545
1546
1547
1548
1549
1550
1551
1552
1553
1554
1555
1556
1557
1558
1559
1560
1561
1562
1563
1564
1565

1566
1567

G.4.2 THE Distances Polynomials REPRESENTATION

1568
1569
1570

It was mentioned that the Distances Polynomials representation is given by non-trivial invariant polynomials computed on top of interatomic distances. These polynomials are constant with respect to changing the order of identical hydrogen atoms.

1571

1572

1573

$$P_1 = x_5 + x_6 + x_7 + x_8 + x_9 + x_{10}$$

1574

$$P_2 = x_1 + x_2 + x_3 + x_4$$

1575

$$P_3 = x_5^2 + x_6^2 + x_7^2 + x_8^2 + x_9^2 + x_{10}^2$$

1576

$$P_4 = x_5x_6 + x_5x_7 + x_6x_7 + x_5x_8 + x_6x_8 + x_5x_9 + x_7x_9 + x_8x_9 + x_6x_{10} + x_7x_{10} + x_8x_{10} + x_9x_{10}$$

1577

$$P_5 = x_1x_5 + x_2x_5 + x_1x_6 + x_3x_6 + x_1x_7 + x_4x_7 + x_2x_8 + x_3x_8 + x_2x_9 + x_4x_9 + x_3x_{10} + x_4x_{10}$$

1578

$$P_6 = x_1^2 + x_2^2 + x_3^2 + x_4^2$$

1579

$$P_7 = x_5^3 + x_6^3 + x_7^3 + x_8^3 + x_9^3 + x_{10}^3$$

1580

$$P_8 = x_5^2x_6 + x_5x_6^2 + x_5^2x_7 + x_6^2x_7 + x_5x_7^2 + x_6x_7^2 + x_5^2x_8 + x_6^2x_8 + x_5x_8^2 + x_6x_8^2 + x_5^2x_9 + x_6x_9^2 + x_7x_9^2 + x_8x_9^2 + x_6^2x_{10} + x_7^2x_{10} + x_8^2x_{10} + x_9^2x_{10} + x_6x_{10}^2 + x_7x_{10}^2 + x_8x_{10}^2 + x_9x_{10}^2$$

1581

$$P_9 = x_1x_5^2 + x_2x_5^2 + x_1x_6^2 + x_3x_6^2 + x_1x_7^2 + x_4x_7^2 + x_2x_8^2 + x_3x_8^2 + x_2x_9^2 + x_4x_9^2 + x_3x_{10}^2 + x_4x_{10}^2$$

1582

$$P_{10} = x_5x_6x_8 + x_5x_7x_9 + x_6x_7x_{10} + x_8x_9x_{10}$$

1583

$$P_{11} = x_1x_5x_6 + x_1x_5x_7 + x_1x_6x_7 + x_2x_5x_8 + x_3x_6x_8 + x_2x_5x_9 + x_4x_7x_9 + x_2x_8x_9 + x_3x_6x_{10} + x_4x_7x_{10} + x_3x_8x_{10} + x_4x_9x_{10}$$

1584

$$P_{12} = x_1^2x_5 + x_2^2x_5 + x_1^2x_6 + x_3^2x_6 + x_1^2x_7 + x_4^2x_7 + x_2^2x_8 + x_3^2x_8 + x_2^2x_9 + x_4^2x_9 + x_3^2x_{10} + x_4^2x_{10}$$

1585

$$P_{13} = x_1x_2x_5 + x_1x_3x_6 + x_1x_4x_7 + x_2x_3x_8 + x_2x_4x_9 + x_3x_4x_{10}$$

1586

$$P_{14} = x_1^3 + x_2^3 + x_3^3 + x_4^3$$

1587

$$P_{15} = x_5^4 + x_6^4 + x_7^4 + x_8^4 + x_9^4 + x_{10}^4$$

1588

$$P_{16} = x_5^3x_6 + x_5x_6^3 + x_5^3x_7 + x_6^3x_7 + x_5x_7^3 + x_6x_7^3 + x_5^3x_8 + x_6x_8^3 +$$

1589

$$x_5x_8^3 + x_6x_8^3 + x_5^3x_9 + x_7^3x_9 + x_8^3x_9 + x_5x_9^3 + x_7x_9^3 + x_8x_9^3 +$$

1590

$$x_6x_{10}^3 + x_7x_{10}^3 + x_8x_{10}^3 + x_9x_{10}^3 + x_6x_{10}^3 + x_7x_{10}^3 + x_8x_{10}^3 + x_9x_{10}^3$$

1591

$$P_{17} = x_1x_5^3 + x_2x_5^3 + x_1x_6^3 + x_3x_6^3 + x_1x_7^3 + x_4x_7^3 + x_2x_8^3 + x_3x_8^3 + x_2x_9^3 + x_4x_9^3 + x_3x_{10}^3 + x_4x_{10}^3$$

1592

$$P_{18} = x_1x_5^2x_6 + x_1x_5x_6^2 + x_1x_5^2x_7 + x_1x_6x_7^2 + x_1x_6x_7^2 + x_2x_5^2x_8 + x_3x_6x_8 +$$

1593

$$x_2x_5x_8^2 + x_3x_6x_8^2 + x_2x_5^2x_9 + x_4x_7x_9 + x_2x_8x_9^2 + x_2x_5x_9^2 + x_4x_7x_9^2 + x_2x_8x_9^2 +$$

1594

$$x_3x_6x_{10}^2 + x_4x_7x_{10}^2 + x_3x_8x_{10}^2 + x_4x_9x_{10}^2 + x_3x_6x_{10}^2 + x_4x_7x_{10}^2 + x_3x_8x_{10}^2 + x_4x_9x_{10}^2$$

1595

$$P_{19} = x_2x_5^2x_6 + x_3x_5x_6^2 + x_2x_5^2x_7 + x_3x_6^2x_7 + x_4x_5x_7^2 + x_4x_6x_7^2 + x_1x_5^2x_8 + x_1x_6^2x_8 +$$

1596

$$x_3x_5x_8^2 + x_2x_6x_8^2 + x_1x_5^2x_9 + x_1x_7^2x_9 + x_3x_8^2x_9 + x_4x_5x_9^2 + x_2x_7x_9^2 + x_4x_8x_9^2 +$$

1597

$$x_1x_6^2x_{10} + x_1x_7^2x_{10} + x_2x_8^2x_{10} + x_2x_9^2x_{10} + x_4x_6x_{10}^2 + x_3x_7x_{10}^2 + x_4x_8x_{10}^2 + x_3x_9x_{10}^2$$

1598

$$P_{20} = x_1^2x_5^2 + x_2^2x_5^2 + x_1^2x_6^2 + x_3^2x_6^2 + x_1^2x_7^2 + x_4^2x_7^2 + x_2^2x_8^2 + x_3^2x_8^2 +$$

1599

$$x_2^2x_9^2 + x_4^2x_9^2 + x_3^2x_{10}^2 + x_4^2x_{10}^2$$

1600

(12)

1619

The exact form of these polynomials is given in Eq. 12 and Eq. 13, where x_1, x_2, \dots, x_{10} correspond to interatomic distances $CH_1, CH_2, CH_3, CH_4, H_1H_2, H_1H_3, H_2H_3$,

1620 H_2H_4 , and H_3H_4 respectively. The presented polynomials form invariant generators (Derksen
 1621 & Kemper, 2015) of the group corresponding to arbitrary permutations of the hydrogen
 1622 atoms. Therefore, the **Distances Polynomials** representation preserves all the information
 1623 about the initial CH_4 molecule.

1624

1625

1626

1627

1628

$$\begin{aligned}
 P_{21} &= x_1x_2x_5^2 + x_1x_3x_6^2 + x_1x_4x_7^2 + x_2x_3x_8^2 + x_2x_4x_9^2 + x_3x_4x_{10}^2 \\
 P_{22} &= x_1^2x_5x_6 + x_1^2x_5x_7 + x_1^2x_6x_7 + x_2^2x_5x_8 + x_3^2x_6x_8 + x_2^2x_5x_9 + x_4^2x_7x_9 + x_2^2x_8x_9 + \\
 &\quad x_3^2x_6x_{10} + x_4^2x_7x_{10} + x_3^2x_8x_{10} + x_4^2x_9x_{10} \\
 P_{23} &= x_1^3x_5 + x_2^3x_5 + x_1^3x_6 + x_3^3x_6 + x_1^3x_7 + x_4^3x_7 + x_2^3x_8 + x_3^3x_8 + \\
 &\quad x_2^3x_9 + x_4^3x_9 + x_3^3x_{10} + x_4^3x_{10} \\
 P_{24} &= x_1^4 + x_2^4 + x_3^4 + x_4^4 \\
 P_{25} &= x_5^5 + x_6^5 + x_7^5 + x_8^5 + x_9^5 + x_{10}^5 \\
 P_{26} &= x_1x_5^4 + x_2x_5^4 + x_1x_6^4 + x_3x_6^4 + x_1x_7^4 + x_4x_7^4 + x_2x_8^4 + x_3x_8^4 + \\
 &\quad x_2x_9^4 + x_4x_9^4 + x_3x_{10}^4 + x_4x_{10}^4 \\
 P_{27} &= x_1x_5^3x_6 + x_1x_5x_6^3 + x_1x_5^3x_7 + x_1x_6^3x_7 + x_1x_5x_7^3 + x_1x_6x_7^3 + x_2x_5^3x_8 + x_3x_6^3x_8 + \\
 &\quad x_2x_5x_8^3 + x_3x_6x_8^3 + x_2x_5^3x_9 + x_4x_7^3x_9 + x_2x_8^3x_9 + x_2x_5x_9^3 + x_4x_7x_9^3 + x_2x_8x_9^3 + \\
 &\quad x_3x_6^3x_{10} + x_4x_7^3x_{10} + x_3x_8^3x_{10} + x_4x_9^3x_{10} + x_3x_6x_{10}^3 + x_4x_7x_{10}^3 + x_3x_8x_{10}^3 + x_4x_9x_{10}^3 \\
 P_{28} &= x_1^2x_5^3 + x_2^2x_5^3 + x_1^2x_6^3 + x_3^2x_6^3 + x_1^2x_7^3 + x_4^2x_7^3 + x_2^2x_8^3 + x_3^2x_8^3 + \\
 &\quad x_2^2x_9^3 + x_4^2x_9^3 + x_3^2x_{10}^3 + x_4^2x_{10}^3 \\
 P_{29} &= x_1x_2x_5^3 + x_1x_3x_6^3 + x_1x_4x_7^3 + x_2x_3x_8^3 + x_2x_4x_9^3 + x_3x_4x_{10}^3 \\
 P_{30} &= x_1^3x_5^2 + x_2^3x_5^2 + x_1^3x_6^2 + x_3^3x_6^2 + x_1^3x_7^2 + x_4^3x_7^2 + x_2^3x_8^2 + x_3^3x_8^2 + \\
 &\quad x_2^3x_9^2 + x_4^3x_9^2 + x_3^3x_{10}^2 + x_4^3x_{10}^2 \\
 P_{31} &= x_1^3x_2x_5 + x_1x_2^3x_5 + x_1^3x_3x_6 + x_1x_3^3x_6 + x_1^3x_4x_7 + x_1x_4^3x_7 + x_2^3x_3x_8 + x_2x_3^3x_8 + \\
 &\quad x_2^3x_4x_9 + x_2x_4^3x_9 + x_3^3x_4x_{10} + x_3x_4^3x_{10}
 \end{aligned} \tag{13}$$

1654

1655

1656

1657

1658

1659 G.5 LMKAN-BASED CONVOLUTIONAL NEURAL NETWORKS

1660

1661

1662 For CIFAR-10, our backbone architecture consists of five 2×2 convolutions, each with stride
 1663 2, and two fully connected layers at the end. Since the resolution of CIFAR-10 images is
 1664 32×32 , where $32 = 2^5$, five 2×2 convolutions with stride 2 transform the spatial dimensions
 1665 of an image exactly to 1×1 . All the layers use the same width (= number of filters in case
 1666 of convolutions, and hidden dimension in case of fully connected layers), which we vary for
 1667 both families of the models. In other aspects, the models are similar to those we employed
 1668 in previous sections - we use batch normalizations with affine transforms for MLP-CNNs,
 1669 and without for LMKAN-CNNs; MLP-CNNs use ReLU activations, while LMKAN-CNNs do
 1670 not require additional activation layers.

1671 The dataset comes with pre-defined full training and test subsets. We split the full training
 1672 subset into training and validation parts in a 90%/10% ratio. Our augmentation pipeline
 1673 consists of established techniques, such as RandAugment Cubuk et al. (2020), MixUp Zhang
 et al. (2017), CutMix Yun et al. (2019), and a few others.

```

1674
1675 CIFAR-10 CNN backbone
1676 # Only convolutional and fully
1677 # connected layers are shown
1678
1679 # [32, 32, 3] → [16, 16, width]
1680 Conv2D(3 → width, kernel_size = 2,
1681 stride = 2)
1682
1683 # [16, 16, width] → [8, 8, width]
1684 Conv2D(width → width, kernel_size =
1685 2, stride = 2)
1686
1687 # [8, 8, width] → [4, 4, width]
1688 Conv2D(width → width, kernel_size =
1689 2, stride = 2)
1690
1691 # [4, 4, width] → [2, 2, width]
1692 Conv2D(width → width, kernel_size =
1693 2, stride = 2)
1694
1695 # [2, 2, width] → [1, 1, width]
1696 Conv2D(width → width, kernel_size =
1697 2, stride = 2)
1698 FullyConnected(width → width)
1699 FullyConnected(width → 10)
1700
1701
1702 ImageNet CNN backbone
1703
1704 # Only convolutional and fully
1705 # connected layers are shown
1706
1707 # [81, 81, 3] → [27, 27, base_width]
1708 Conv2D(3 → base_width, kernel_size =
1709 3, stride = 3)
1710
1711 # [27, 27, base_width] → [9, 9, 3*
1712 # base_width]
1713 Conv2D(base_width → 3*base_width,
1714 kernel_size = 3, stride = 3)
1715
1716 # [9, 9, 3*base_width] → [3, 3, 9*
1717 # base_width]
1718 Conv2D(3*base_width → 9*base_width,
1719 kernel_size = 3, stride = 3)
1720
1721 # [3, 3, 9*base_width] → [1, 1, 27*
1722 # base_width]
1723 Conv2D(9*base_width → 27*base_width,
1724 kernel_size = 3, stride = 3)
1725
1726 FullyConnected(27*base_width → 27*
1727 base_width)
1728 FullyConnected(27*base_width → 1000)
1729
1730

```

Figure 25: CIFAR-10 and ImageNet CNN backbones. MLP-based CNNs additionally have ReLU activations and batch normalizations with enabled affine transforms. ImKAN-based CNNs do not require additional activations and use batch normalizations without affine transforms as suggested by our sigma grids described in Sec. 3.1.

We use the following pool of augmentations for the CIFAR-10 dataset:

```

1706 CIFAR-10 augmentation pipeline
1707
1708 MEAN = (0.4914, 0.4822, 0.4465)
1709 STD = (0.2470, 0.2435, 0.2616)
1710
1711 nn.Sequential(
1712     T.RandomCrop(32, padding=4),
1713     T.RandomHorizontalFlip(),
1714     T.ColorJitter(0.3, 0.3, 0.3, 0.05),
1715     T.RandAugment(2, 7),
1716     T.RandomErasing(p=0.25, scale=(0.05, 0.2), ratio=(0.3, 3.3)),
1717     T.Normalize(MEAN, STD),
1718 )

```

On top of these, we use MixUp (Zhang et al., 2017) ($\alpha = 0.2$) and CutMix (Yun et al., 2019) ($\beta = 1.0$) augmentations, both with 50% probability.

When fitting the families of convolutional neural networks described in the main text, we use the above pool of augmentations consistently for MLP-based and ImKAN-based CNNs.

For ImageNet, the standard data preparation pipeline introduced by AlexNet (Krizhevsky et al., 2012) involves first resizing an image to 256 pixels along the smallest dimension, then performing a random crop of 224×224 pixels during training, and a center crop of 224×224 pixels during validation.

We mimic this procedure by first resizing the image to $81 \cdot 256/224 \approx 93$ pixels across the smallest dimension, and then performing random or center crops of 81×81 pixels.

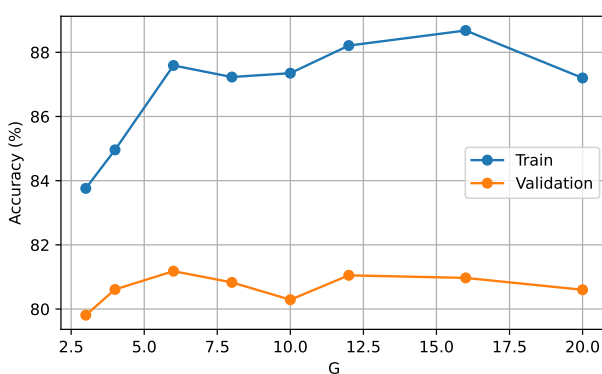


Figure 26: Accuracy of the lmKAN-based CNNs on the CIFAR-10 dataset depending on the grid resolution G .

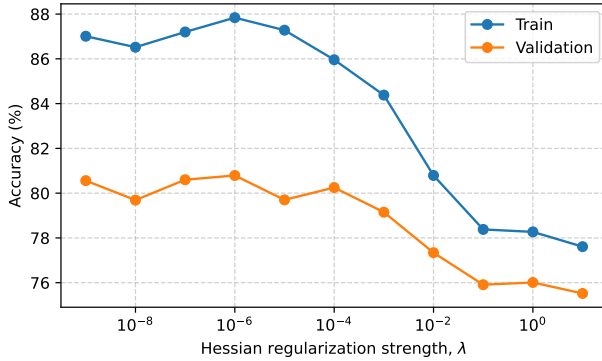


Figure 27: Accuracy of the lmKAN-based CNNs on the CIFAR-10 dataset depending on the strength of Hessian regularization.

Next, we use the following augmentation pipeline:

ImageNet augmentation pipeline

```
nn.Sequential(
    T.RandomHorizontalFlip(),
    T.ColorJitter(brightness=0.4, contrast=0.4, saturation=0.4, hue=0.1),
    T.RandAugment(),
    T.RandomErasing(p=0.25, scale=(0.02, 0.33), ratio=(0.3, 3.3), value=0),
    T.Normalize(mean=[0.485, 0.456, 0.406], std=[0.229, 0.224, 0.225]),
)
```

On top of these, we use MixUp and CutMix.

G.6 COMPARISON WITH FASTKAN

As was already mentioned in the main text, we use the training script for the CIFAR-10 dataset available in the FastKAN GitHub repository (Li, 2024a) as the basis for the comparison of lmKAN and FastKAN. However, we provide several modifications to the pipeline.

The original script implements the fitting procedure of a fully connected FastKAN model on the CIFAR-10 dataset without augmentations. The model has only one hidden layer

1782 with 256 neurons. Without augmentations, it overfits the data quickly. Thus, the very short
1783 fitting procedure in the original script is sufficient.
1784
1785 We extend the script by the same augmentation pipeline as we used in Sec. 4.3 for the
1786 CIFAR-10 dataset. We observed that because of augmentations, one has to fit the model
1787 for a longer time, so the training budget was substantially increased. The data was split
1788 properly into train, validation, and test subsets, while the original script employed only a
1789 train-validation split. We use the cosine (without restarts) learning rate scheduler (Loshchilov
1790 & Hutter, 2016) instead of the exponential decay one in the original script. Finally, the
1791 normalization was performed with real values of the mean and standard deviation for the
1792 CIFAR-10 dataset, instead of the dummy 0.5 values of the original script.
1793 These modifications significantly improve the performance of FastKAN models ($\approx 54 - 55\%$
1794 validation accuracy in the original script), see Fig. 9. Furthermore, even the MLP baseline of
1795 the same shape yields better accuracy compared to the performance of the FastKAN model
1796 in the original script.
1797
1798
1799
1800
1801
1802
1803
1804
1805
1806
1807
1808
1809
1810
1811
1812
1813
1814
1815
1816
1817
1818
1819
1820
1821
1822
1823
1824
1825
1826
1827
1828
1829
1830
1831
1832
1833
1834
1835